Technical opportunities and challenges in developing total-body PET scanners for mice and rats

Junwei Du[1*] and Terry Jones[2*]

*Correspondence:
jwdu@ucdavis.edu; terry.
jones40@googlemail.com

[1] Department of Biomedical Engineering, University of California at Davis, Davis, CA 95616, USA
[2] Department of Radiology, University of California at Davis, Davis, CA 95616, USA

Abstract

Positron emission tomography (PET) is the most sensitive in vivo molecular imaging technique available. Small animal PET has been widely used in studying pharmaceutical biodistribution and disease progression over time by imaging a wide range of biological processes. However, it remains true that almost all small animal PET studies using mouse or rat as preclinical models are either limited by the spatial resolution or the sensitivity (especially for dynamic studies), or both, reducing the quantitative accuracy and quantitative precision of the results. Total-body small animal PET scanners, which have axial lengths longer than the nose-to-anus length of the mouse/rat and can provide high sensitivity across the entire body of mouse/rat, can realize new opportunities for small animal PET. This article aims to discuss the technical opportunities and challenges in developing total-body small animal PET scanners for mice and rats.

Keywords: Total-body PET, Small animal, Mice, Rat

Introduction

Because of the pathophysiological similarities between vertebrate mammals and humans, vertebrate mammals are widely used as models to study human disease and functions [1–7]. Mouse and rat comprise approximately 99.3% of mammals used in preclinical research in the USA [8]. Hence, small animal positron emission tomography (PET) scanners, which have small diameters to obtain high spatial resolution to image the small amount of radiation tracer distributed within small structures of the animal body, were designed in the 1990s, starting with the microPET [9]. Now, some hundreds of small animal positron emission tomography (PET) scanners are installed worldwide. Most major academic medical research centers and pharmaceutical companies have access to and routinely use this technology. Key characteristics of small-animal PET are spatial resolution and sensitivity, which strongly affect the quantitative accuracy and precision of PET imaging. However, it remains true that almost all small animal PET studies using mouse or rat as models are either limited by the spatial resolution or the sensitivity (especially for dynamic studies), or both, reducing the quantitative accuracy
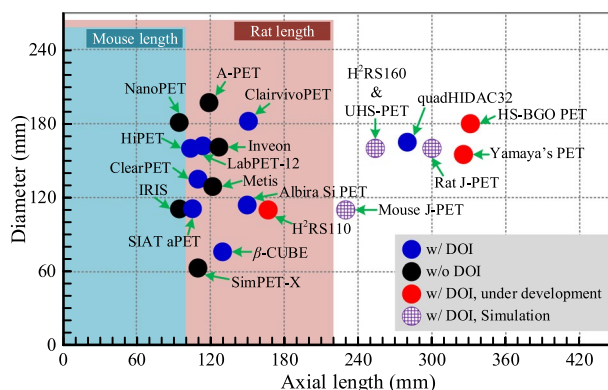
Fig. 1 Axial length and diameter of small animal scanners with axial lengths longer than 90 mm [13, 21, 28–31, 38, 40–48]. Only scanners with published results were selected. References of the scanners are shown in Table 3

and quantitative precision of the results. Furthermore, few scanners have been designed to cover the whole body of the mouse or rat with equal sensitivity [10–13]. Hence, few offer the opportunity to undertake interactive "systems" studies of the whole body using simultaneous kinetic time course for the whole tissues of the body. Such pre-clinical studies are destined to support the development of human total-body PET scanner-based applications by developing and characterizing suitable paradigms [14–17].

Quantitative accuracy is strongly linked with spatial resolution through the partial volume effect, the single largest quantitative error in almost all small animal PET studies [18]. Improving spatial resolution reduces the partial volume effect, thus improving accuracy. Quantitative precision is strongly linked with the number of detected events through the statistical uncertainties that are governed by Poisson counting statistics. Increasing the scanner sensitivity increases the number of detected events, thus increasing the precision of PET measurements. A further benefit of higher sensitivity is that it permits faster dynamic imaging, i.e., increasing temporal resolution [14, 19, 20], which can benefit quantification through improved temporal data to feed into tracer kinetic models, such as in measuring the image-derived input function (IDIF) from a major arterial vessel, i.e., aorta.

The sensitivity of PET scanners can be dramatically increased by increasing the geometric coverage to cover the entire body of the subject [12, 21], using thick crystals with high stopping power, and reducing the gap between detector elements [22–24, 24]. To obtain high uniform resolution across the field-of-view (FOV), high spatial resolution detectors with the ability to record depth-of-interaction (DOI) information are needed [11, 12, 25]. In this article, we will discuss the technical opportunities and challenges in developing optimal total-body small animal PET scanners for mice and rats.

Status of current total-body small-animal PET

The axial lengths and diameters of currently available small animal PET scanners with axial lengths longer than 90 mm, together with these under construction and proposed with simulation results, are shown in Fig. 1, while their resolution and sensitivity are shown in Fig. 2. (Only scanners with published results were selected. References of the scanners are shown in Table 3.). Almost all state-of-the-art scanners have an axial length
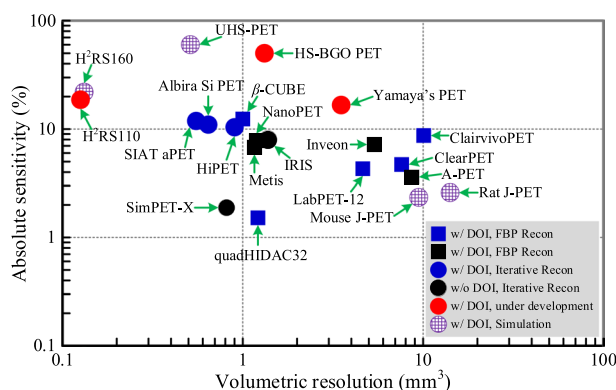
Fig. 2 Volumetric resolution and sensitivity at the center of small animal scanners with axial lengths longer than 90 mm [13, 21, 28–31, 38, 40–48], which corresponds to Fig. 1. Only scanners with published results were selected. References of the scanners are shown in Table 3

longer than the nose-to-anus length of the mouse, which can be up to 10 cm [26]. However, all the currently available scanners, except the quadHIDAC32, have axial lengths shorter than the nose-to-anus length of the rat, which can be up to 20 cm [27].

The four latest small animal scanners, the β-CUBE, the Albira Si PET, the HiPET, and the SIAT aPET scanners, are all built with DOI detectors and have ∼10% sensitivities, as measured for a point source at the center of the scanner, and better than the 1 mm resolution. To obtain high spatial resolution across the FOV, all these four scanners are based on detectors with DOI information to reduce the parallax error. The β-CUBE PET scanner incorporates a detector design that comprises a $25.4 \times 25.4 \times 8$ mm^3 thick monolithic lutetium–yttrium oxyorthosilicate (LYSO) scintillator block coupled to an array of 3.0×3.0 mm^2 Hamamatsu silicon photomultipliers (SiPMs) [28]. A maximum likelihood (ML) clustering algorithm was used to estimate the 3D location of each gamma interaction within the crystals of PET detectors. The detectors have a 1.6 mm DOI resolution. This scanner, with a 76 mm ring diameter and 130 mm axial length, has a 1.1 mm spatial resolution (3D filtered back projection (FBP) reconstruction algorithm) and 12.4% sensitivity (255–765 keV energy window (EW)) at the center of the scanner. The Albira Si PET scanner uses $50 \times 50 \times 10$ mm^3 monolithic LYSO scintillator blocks coupled to SiPM arrays of 3×3 mm^2 SiPM elements [29]. The scanner has a 114 mm ring diameter, and a 150 mm axial length, and the detectors have around 1.6 mm DOI resolution. The spatial resolution and sensitivity of the scanner are ∼1 mm (maximum likelihood expectation maximization (MLEM) reconstruction algorithm) and 11.0% at the center of the scanner, respectively. The HiPET scanner is built with dual-layer scintillator arrays based on LYSO and BGO to provide two-layer DOI information [30]. Each scintillator array consists of a front layer, a 48×48 LYSO array of $1.01 \times 1.01 \times 6.1$ mm^3 crystal elements (1.09 mm pitch size), and a back layer, a 32×32 bismuth germanate (BGO) array of $1.55 \times 1.55 \times 8.9$ mm^3 elements (1.63 mm pitch size). The back layer is coupled to Hamamatsu H12700 flat panel multi-anode photomultiplier tube (MAPMT). The HiPET has a 160 mm ring diameter and 104 mm axial length. The spatial resolution is 0.93 mm (3D ordered subset expectation maximization (OSEM) reconstruction algorithm), and the sensitivity is 10.4% (350–650 keV EW) at the center of the scanner.

The SIAT aPET is built using dual-ended readout detectors consisting of Hamamatsu S13361-3050-08 SiPM arrays coupled to both ends of LYSO arrays of $1.0 \times 1.0 \times 20$ mm^3 crystal elements (1.07 mm pitch). This scanner has a 116 mm ring diameter and 105.6 mm axial length. The DOI resolutions of the detectors are around 1.96 mm. The spatial resolution and sensitivity of the scanner are 0.8 mm (3D OSEM reconstruction algorithm) and 11.9% (350–750 keV EW), respectively, at the center of the scanner.

However, as shown in Fig. 3, although the HiPET and SIAT aPET scanners have axial lengths slightly longer than the nose-to-anus length of the mouse, they cannot perform total-body studies due to the significant fall-off of sensitivities at the two ends of the scanners [30, 31]. Two-bed positions are needed to image the mouse, and three-bed positions are needed for a rat scan. The β-CUBE and the Albira Si PET scanners can provide higher than 5% sensitivity for the nose and anus with a mouse located at the center of the scanner. Although a sensitivity compromise, they do offer the means to undertake total-body mouse studies.

Among the mice and rats used in the USA, 97.3% of them are mice and 2.7% are rats [8]. Hence, most small animal PET scanners are designed for undertaking mouse studies. However, rats are preferred for studies of the brain due to the larger size of rats and the resolution limitation of currently available PET scanners (Fig. 2) [12, 32–36]. Until recently, the only scanner built to date that can cover the entire rat body is the quadHIDAC32 PET scanner, which has a 280 mm axial length and 165 mm ring diameter [37–39]. The quadHIDC32 PET scanner that was built around 2005 using multiwire proportional chambers (MWPCs) and is still operational has four detector banks arranged in a box shape. Each detector bank has eight separate chambers stacked together to improve the sensitivity and provide a 2.5 mm DOI information, which maintains the spatial resolution across the FOV of the scanner [39]. It has a ~ 1.0 mm resolution (FBP reconstruction algorithm). However, the sensitivity is only 1.5% for a point source located at the center of the scanner, which is much lower than most of the other scanners. The low sensitivity limits the application of the scanner to static PET studies only [38].
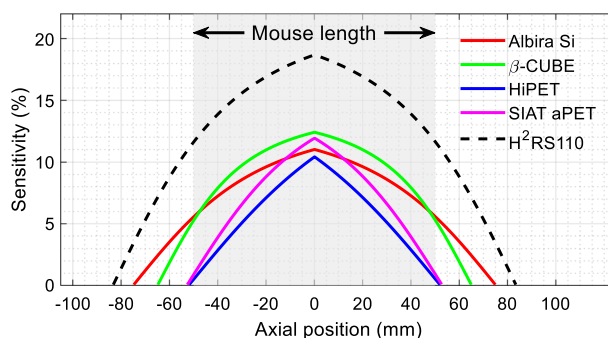

Fig. 3 Sensitivity of small animal scanners that can perform mouse studies and have axial FOVs longer than 100 mm. The sensitivities were estimated using the solid angle coverage, and the sensitivities at the center of the scanners are reported using the published data. Note the need to extend the axial length of the scanner beyond the length of the mouse to ensure sufficient sensitivity as realized at the two ends of the animal
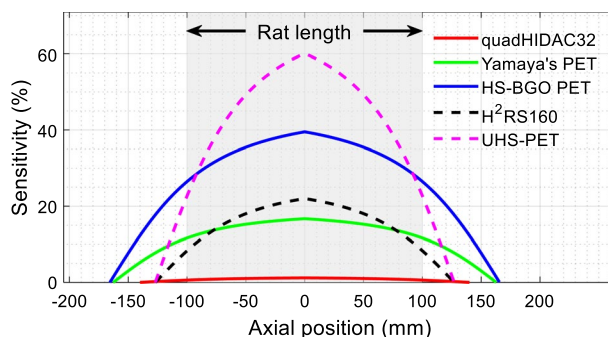
Fig. 4 Sensitivity of small animal scanners that can perform both total-body rat and total-body mouse studies. The sensitivities were estimated using the solid angle coverage, and the sensitivities at the center of the scanners were reported using the published data. Note the need to extend the axial length of the scanner beyond the length of the rat to ensure sufficient sensitivity as realized at the two ends of the animal
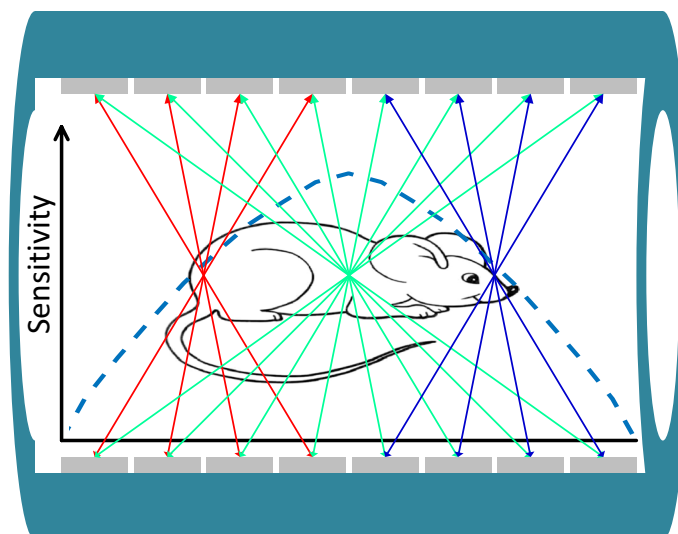

Fig. 5 Total-body small animal PET scanners need to have an axial length longer than the length of the mice/rats to maximize sensitivity across the entire body of the animals. The PET scanner (H²RS110) shown in this figure, which is designed for total-body mouse studies only, has a 110 mm ring diameter and 167 mm axial length [12]

Total-body small-animal PET for mouse and rat

The function of the PET scanner is to detect the coincident "back-to-back" 511-keV photons that are produced when a positron interacts with an electron [18]. Due to the radiation being emitted isotopically, state-of-the-art PET scanners are all operated in the three-dimensional data acquisition mode to achieve high sensitivity. In three-dimensional mode, the axial sensitivity profile is determined geometrically, which peaks at the center of the scanner and reduces to zero at the two ends of the scanner (Figs. 3, 4, 5) [12, 18]. Hence, to maximize sensitivity for the entire body of the animal, the axial length of the scanner needs to be extended beyond the length of the animals, such as the mouse and the rat, to image the animals using a one bed position for total-body studies (Fig. 5).

Current developments of total-body small-animal PET

To further increase the performance, especially sensitivity for mouse/rat studies, to our knowledge, up to the moment this review is prepared, six total-body small animal PET scanners are either under development or proposed with simulation results.

Groups from the University of California at Davis and the University of Texas Arlington have proposed a design to build a scanner with a 110 mm ring diameter and 167 mm axial length for total-body mouse studies (Fig. 5) [12]. This scanner is based on dual-ended readout detectors based on position-sensitive SiPMs (PS-SiPMs) coupled to both ends of 20 mm thick LYSO arrays (H^2RS110 shown in Figs. 1, 2, 3) [12, 51, 52]. Besides increasing the sensitivity, LYSO arrays of $0.44 \times 0.44 \times 20$ mm^3 crystal elements (0.5 mm pitch size) are used to achieve the physical limits of spatial resolution that could be obtained from coincidence detection. The DOI resolution of the detectors is ∼2 mm [53]. Monte Carlo simulation results show that this scanner can provide ∼18.7% sensitivity (250–750 keV EW) at the center of the scanner and better than 10% sensitivity across the entire mouse body. The resolution is ∼0.5 mm across the whole mouse body, obtained using the MLEM reconstruction algorithm [12].

In Dr. Yamaya's Lab in Japan, a scanner with a 153 mm ring diameter and 325.6 mm axial length is under construction using four-layer Zr-doped gadolinium oxyorthosilicate (GSOZ) crystal arrays of $2.8 \times 2.8 \times 7.5$ mm^3 crystal elements [21]. The pitch size of the GSOZ arrays is 2.85 mm, and Hamamatsu H8500 position-sensitive PMTs are used as photodetectors. Depth of interaction is determined using a light-sharing method in which the optical photon distributions arriving at the PMT are modified via the insertion of radial reflectors in the crystal array with different patterns for each layer, providing a 7.5 mm DOI information [54, 55]. The measured sensitivity is 16.7% at the center of the scanner using a 400–600 keV energy window. The spatial resolutions at the center and 30 mm radial offset are 1.52 mm and 1.75 mm, respectively, obtained using OSEM reconstruction algorithm. Due to GSOZ arrays with a large pitch size are used, the spatial resolution of this scanner is worse than most of the state-of-the-art scanners (Fig. 2), such as the β-CUBE and the Albira Si PET scanners.

At the University of California at Davis, we are also building a similar axial length but wider bore scanner with a diameter of 180 mm and axial length of 331.2 mm (HS-BGO PET in Figs. 1, 2, 4) [49]. Dual-ended readout detectors are used based on 32×32 BGO arrays with a 1.6 mm pitch size and 20 mm thickness [56]. BGO scintillator, instead of widely used L(Y)SO, is selected for very-low-dose PET imaging. Compared to L(Y)SO, BGO has much lower intrinsic radiation [57], higher stopping power, and higher photoelectronic ratio [18, 58, 59]. These make BGO a better choice for high sensitivity small animal PET scanners, especially for very-low-dose studies, such as cell tracking using long lived radionuclides [60, 61] and gene expression [62–64]. The lower cost of BGO will also make the scanner more affordable. The measured results show that the detector has a ∼3.2 mm DOI resolution [56]. From the Monte-Carlo simulation, the sensitivity of the scanner is 39.5% at the center of the scanner (250–625 keV EW), and higher than 20% within the 200 mm axial center region for rat studies, and higher than 30% within the 100 mm axial center region for mouse studies (Fig. 4). The spatial resolution is ∼1.1 mm across the entire mouse/rat body. However, due to the slower decay time of

BGO and the larger size of the detector module, the peak count rate is low, which makes the scanner a good choice principally for low activity studies.

The HS-BGO PET scanner is designed to work optimally for studies with body loads of radioactivity lower than 50 uCi (1.85 MBq). This is due to the large size of the detector (51.2×51.2 mm^2), the slow decay time of the BGO, and the signal multiplexing readout which is chosen to simplify the readout electronics [65]. To build PET scanners that can be used both for total-body mouse and rat studies, and have high resolution and high sensitivity simultaneously, we also proposed to build two high performance PET scanners (H^{2}RS160 and UHS-PET scanners shown in Figs. 1, 2, 4) that can work with high injected dose. They both have a diameter of 160 mm and axial length of 254 mm and are based on dual-ended readout detectors to obtain DOI information. The H^{2}RS160 PET scanner is based on linearly graded SiPM (LG-SiPM, a type of PS-SiPM) arrays coupled to both ends of LYSO arrays with a 0.5 mm pitch size and 20 mm thickness [12, 52]. The DOI resolution of the detectors is ~ 2.0 mm [31]. The Monte Carlo simulation results show that the H^{2}RS160 PET has 22% sensitivity (250–750 keV EW) at the center of the scanner. The sensitivity across the mouse body is higher than 16%, and it is higher than 7% across the entire rat body. The spatial resolution obtained using the MLEM reconstruction algorithm is ~ 0.5 mm across the mouse/rat bodies. The UHS-PET scanner is based on our recently developed curved LYSO arrays with a 1.0 mm pitch size on the inner side and 30 mm thickness [22, 66]. The curved LYSO arrays were developed to reduce the dead space between detector modules in PET scanners with conventional cuboid scintillator arrays, and thereby the sensitivity can be significantly improved (Fig. 7). The dual-ended readout method was also used to obtain a ~ 2.8 mm DOI resolution from 30 mm thick LYSO [22]. Based on the measured detector results, Monte Carlo simulation shows that the scanner can provide a ~ 0.8 mm spatial resolution across the mouse/rat body using the MLEM reconstruction algorithm. The sensitivity is 60.1% (250–750 keV EW) at the center of the scanner, and it is higher than 45% across the mouse body and higher than 20% across the rat body [50].

To build cost-effective total-PET scanners, researchers at the Jagiellonian University introduced plastic scintillator based PET scanners (J-PET) [67, 68]. Opposed to the traditional PET design concept, J-PET uses axially arranged detection units, each consisting of a plastic scintillator strip readout with silicon photomultipliers on both ends. Although the J-PET technology was initially developed for clinical PET scanners, recently, the sensitivity of a total-body mouse J-PET and a total-body rat J-PET were simulated using the GATE software [48]. The mouse J-PET scanner is based on $1 \times 1 \times 230$ mm^3 EJ-230 plastic scintillators, and has a ring diameter of 110 mm and an axial length of 230 mm. The rat J-PET scanner is based on $1 \times 1 \times 300$ mm^3 EJ-230 plastic scintillators, and has a ring diameter of 160 mm and an axial length of 300 mm. The volumetric spatial resolutions of the mouse J-PET and rat J-PET are 9.5 mm^3 and 14.1 mm^3, respectively. The sensitivities at the center of the FOV of the mouse J-PET and rat J-PET are 2.35% and 2.6%, respectively. These spatial resolutions and sensitivities are lower than those of the scanners described above. The low sensitivities are mainly caused by the low intrinsic stopping power of the EJ-230 plastic scintillator. Although the mouse J-PET and rat J-PET have large FOVs to cover the entire body of mice and rats, the low sensitivity could be a limitation for dynamic studies and for imaging low level of tracer. To

improve the sensitivity, one possibility would be to stack more detector modules in the radial direction.

Opportunities for total-body small-animal PET

The limitations of scanners with short axial FOV

Small animal PET scanners with short axial lengths have lower cost, which are cost effective tools to obtain dynamic or static images of pre-selected regions of the animals [69, 70], or to obtain total-body static images of the entire mouse/rat using multi-bed approaches [31]. However, the drawbacks of the scanners with short axial FOV are also obvious: (1) they cannot, or at least cannot easily perform total-body dynamic imaging and hence the creation of total-body functional parametric images [71], (2) they minimize the opportunity for studying in real time across body interactions, and (3) their sensitivity is usually low due to the small solid angle coverage [10–12].

Total-body image

Total-body imaging using one bed position is required for applications in which the temporal distribution of radiotracer in the entire body or multiple organ systems is of interest. It provides the means to obtain the arterial image derived input function (IDIF) from the heart or aorta, which will be within the FOV of the scanner all the time. This cannot be done, or at least cannot be easily done, using multi-bed dynamic imaging in small animal studies and will certainly compromise the ability to obtain high image quality [72, 73]. Another example is the opportunities for systems biology research [16, 74, 75] which, although still in its infancy, has the prospects for undertaking new areas of biological research. However, to explore the broad scope for such investigations, there is clearly a need to first characterize/validate such pilots at the pre-clinical level. In the systems biology approach, multi-organs need to be imaged simultaneously to study the interactions between different organs such as the brain-gut, and brain–heart. It is envisaged that pre-clinical small animal PET-based developments, including the formulation of investigative paradigms and protocols, could be undertaken to develop and validate new kinetic models for quantifying these interactions.

Low sensitivity

The signal-to-noise ratio (SNR) of the image is determined by the number of detected events. Low sensitivity is the main limitation, especially for realizing high-resolution and dynamic imaging studies with tracer kinetic modeling, because short-time-frame datasets are always statistically limited. To obtain sufficient events, injection doses of high levels of radiolabeled tracer and/or long acquisition time are requested [69, 76], especially for multi-bed static imaging or dynamic imaging. However, to compensate for this, high levels of a radiolabeled tracer especially those produced with low specific activity, namely where there are associated large levels of cold compound, cannot be used. As is could no longer be considered, a procedure adheres to the tracer principle, in which the physical amount of tracer does not perturb the biological process being traced, and could lead to physiologic effects and nonlinear kinetics [77, 78]. The key purpose of developing small animal PET scanners is to study the disease models that can be translated to

human later. To have the similar physiologic effects, many studies suggest that the radiopharmaceutical injection dose be scaled either by the body weight or by the body surface area [79]. In human studies, the typical injected fluorodeoxyglucose (FDG) dose is around 10 mCi. If assuming the patient is 175 cm tall, to have a similar physiologic effect, the injected does scaled down by body weight for a 10 cm long mouse should be around 1/5000 of that for human, which is ~2 μCi, far less than the ~200 μCi injected doses widely used for mouse studies nowadays. However, if a small animal (mouse or rat) and clinical PET study are to be "equivalent" from an imaging point of view, the same coincidence rate must be observed from a small animal image voxel as from a clinical image voxel [77]. The spatial resolution of state-of-the-art clinical PET scanners is ~3 mm; hence, for small animal PET scanners with ~1-mm spatial resolution, the sensitivity of the small animal PET scanners should be 27 times of those of the clinical PET scanners. Most of the clinical PET scanners with < 30 cm axial FOV have ~1 to 2% sensitivity [80–83]. Hence, small animal PET scanners should ideally have a sensitivity better than 50%, which is far beyond the ~10% sensitivity of currently available small animal PET scanners (Fig. 2). One effective way to increase the sensitivity and reduce the injected dose is to increase the solid angle coverage by increasing the axial FOV of the scanner [19].

The benefits of total-body small animal PET to applications

All studies based on mice and rats as models can benefit from the high sensitivity and large geometric coverage of total-body small animal PET scanners. With the improved sensitivity, we can obtain better image quality, or use shorter scan time or less radiation dose, or image the animal over extended time periods [19, 20, 84–86]. Examples are fast dynamic imaging to study the time courses of a label in tissue regions of interest and in arterial blood [20], and studies of chronic inflammatory disease where the binding of translocator protein (TSPO) ligands can be low and hard to detect [87–89]. Another key stimulus for realizing increased sensitivity is the limitation as to the amount of tracer that can be administered of molecules that are with selectivity to specific cellular binding sites. Since it is important to maintain the tracer principle, it is clearly necessary to ensure the amount of the carrier molecules administered along with the radiolabeled molecule does not perturb those binding sites. In effect, there will often be limits as to how much tracer and its accompanying carrier molecule can be administered [90]. Hence, the need for high detection sensitivity to ensure proficient studies can be undertaken in the laboratory mouse or rat in the presence of the described restrictions.

Meanwhile, studies using the recently developed human total-body EXPLORER PET scanner have shown the benefits of total-body PET scanning using one-bed position [20, 86, 91], which are pushing human PET scanning to a new level. Several EXPLORER scanners have been installed, and more long axial FOV human scanners are under development [15, 92, 93]. Total-body PET scanners are destined to affect a step change in the application of PET based molecular imaging in clinical research and healthcare. They represent the only radiological technology that is able to simultaneously image the whole of the human body. Based upon the tracer principal to measure regional tissue function, the means is offered for undertaking a "systems" study of the human by relating for example how specific tissues functionally interact in health, disease and in response to therapy. It is foreseen that such system research studies are destined to impact key areas

such as the immune therapy of cancer, viral immunity, drug development through pharmacokinetics and pharmacodynamics studies, brain-body interactions, auto immune conditions, and cardiovascular disease.

Several high-resolution and high-sensitivity human brain PET scanners are also under development for improving human brain imaging [94–97]. Both human total-body PET, the applications of which are still in their infancy, and more established brain PET need a homologous pre-clinical tool using mouse or rat models to develop, validate, and characterize the paradigms and protocols that can be translated into human PET studies, which are currently unavailable.

Total-body small animal PET scanners can provide high sensitivity across the entire body of mouse/rat with high spatial resolution, thereby providing new opportunities for small animal PET research, and/or opening new windows to using PET for currently unknown applications. Overall, advanced scientific tools offer higher opportunities for exploratory studies.

Image-derived input function

One emerging example of the application of high-resolution and high-sensitivity total-body small animal PET is to obtain the noninvasive IDIF for kinetic modeling. Kinetic modeling with dynamic PET provides sophisticated quantitation of the tracer kinetics with improved prognostic and predictive values over those of simple standard uptake value (SUV) measurements [98–100]. The arterial input function, which describes the time-activity curve of the radiotracer in the blood, is a prerequisite for kinetic modeling. The input function can be derived using arterial blood sampling, which is the conventional method [101]. However, because of the limited blood volume of mouse and rat, the related difficulties in withdrawing blood, and the effects of the accrual rates of the animals, IDIF is an elegant and alternative way, which can be derived from the dynamic images of the arterial blood pools included in the field-of-view of PET [98, 99]. For mouse or rat based studies, the most reliable blood pools for IDIF measurements are the left ventricle and atrium, and ascending or descending aorta, which are the larger blood pools but inside mouse or rat, the sizes are very small [102]. To image these blood pools with a high efficiency during the dynamic studies, the PET scanners need to have high sensitivity which can be derived from an axial field-of-view that is longer than the length of the animals. To reduce the partial volume effect (PVE), spill in and spill out from surrounding tissues of the blood pool and thereby increase the quantitation accuracy and precision of the IDIF [103], both high spatial resolution and high sensitivity are required. This is especially the case for the early time points of a kinetic study, where there are fast changing concentrations of tracer within the blood pool and at the later time points where the levels are low.

Advancing the technology of small animal imaging

The performance of the PET scanner is mainly dominated by the detectors and the readout electronics. During the past 2 decades, both the detector technologies and readout electronics have changed rapidly, which opens the door for high-performance small animal PET scanners.

PET detector

Different types of detectors have been developed [18], including scintillator- and photo-detector-based detectors [21, 104–106], semiconductor-based detectors [107–109], and gas detectors [38, 110, 111]. Semiconductor-based detectors have good energy resolution; however, their timing resolutions are poor, in tens of nano-second [108, 112]. Cerenkov photondetection has been proposed to improve the timing resolution. However, because of the limited numbers of emitted Cerenkov photons which typically for BGO is around 15, it is still in the early stage, and not ready for use at the scanner level, or even at the detector level [113, 114]. The major problem of gas detectors, such as the multigap resistive plate chamber (MRPC) and MWPC, is their low detection efficiency, even when several detectors are stacked together [38]. Its timing resolution and energy resolution also cannot compete with scintillator- and photodetector-based detectors [115–117]. Hence, most of the state-of-the-art PET scanners are based on scintillator- and photodetector-based detectors [19, 28, 30, 31, 93, 118, 119].

Scintillator

The emergence of LSO in 1992 revolutionized the PET scanner in various aspects [11, 120]. The first small animal PET, the microPET developed in the middle of 1990s, was the first to take advantage of the LSO scintillator. Among all the scintillators used in PET today, LSO and LYSO (a variation of LSO), which have similar characteristics, are still the best choice for most applications. This is due to their high density, high

Table 1 Peak noise equivalent count rates (NECRs), system type, and references of scanners shown in Figs. 1 and 2

Name of scanner	Peak NECR (kcps)		System type	References
	Mouse phantom	Rat phantom		
NanoPET	430	130	PET/CT	[45]
A-PET	~500	~230	Standalone	[40]
Inveon	1670	590	PET/CT	[43]
Metis	1344	640	PET/CT	[47]
IRIS	185	40	PET/CT	[46]
ClairvivoPET	415 kcps (50 mm ^{18}F line source)		Standalone	[41]
HiPET	179	63	Standalone	[30]
LabPET-12	362	156	PET/CT	[42]
ClearPET	Unknown	Unknown	PET/CT	[44]
Albira Si PET	486	239	PET/SPECT/CT	[29]
SIAT aPET	324	144	MR-Compatible	[31]
β-CUBE	300	160	PET/CT	[28]
SimPET-X	348	Unknown	MR-Compatible	[13]
quadHIDAC32	67	52	Standalone	[38]
Yamaya's PET	Unknown	Unknown	Standalone	[21]
Mouse J-PET	Unknown	Unknown	Unknown	[48]
Rat J-PET	Unknown	Unknown	Unknown	[48]
HS-BGO PET	Unknown	Unknown	MR-Compatible	[49]
H^{2}RS110	Unknown	Unknown	MR-Compatible	[12]
H^{2}RS160	Unknown	Unknown	Unknown	[12]
UHS-PET	Unknown	Unknown	Unknown	[50]

Table 2 Properties of part scintillators used in PET [18, 123]

Properties	BGO	L(Y)SO	GSO	GAGG[a]
Density (g/cc)	7.1	7.4	6.7	6.6
Effective atomic number	73	66	59	–
Decay time (ns)	300	40	60	50–150
Light yield (photons/MeV)	8000	20,000–30,000	12,000–15,000	30,000–50,000
Attenuation length at 511 keV (mm)	10.4	11.4	14.1	–
Photoelectric fraction (%)	40	32	25	–
Index of refraction	2.15	1.82	1.85	1.91
Peak emission (nm)	480	420	430	520–530
Intrinsic radiation	No	Yes	No	No

[a] Date from https://www.epic-crystal.com/oxide-scintillators/gagg-ce-scintillator.html. GAGG with different components shows different performances

Fig. 6 LYSO arrays with different pitch sizes. (left) 1.0 mm pitch size, (middle) 0.75 mm pitch size, and (right) 0.5 mm pitch size [52, 128, 129]

light yield, high stopping power, and fast decay time (Table 1), which can provide the overall best trade-off between spatial resolution, timing resolution, and energy resolution. However, due to the intrinsic radiation caused by [176]Lu [57, 121, 122], scanners based on LSO and LYSO are not an ideal choice for ultra-low activity studies. BGO, due to its much lower intrinsic radiation and slightly higher stopping power and photoelectric fraction (Table 2), is a better choice for scanners aiming for low activity imaging.

Scintillator array Scintillator arrays used in high-resolution small animal PET scanners always have a pitch size smaller than ~ 1 mm [69, 70, 119]. Much effort has been spent by different researchers to optimize the scintillator arrays, such as the surface treatment [56, 124, 125], the reflector [53, 124, 125], and the array fabrication method [126, 127]. At the University of California at Davis, during the past 20 years, working with different companies, we have optimized the fabrication method and fabricated different scintillator arrays with pitch sizes down to 0.25 mm (Fig. 6) [52, 128, 129] using different materials [52, 56, 130] and with different shapes (Fig. 7) [22, 130, 131]. Now, we can fabricate high-quality scintillator arrays with small pitch sizes for different applications.

Monolithic scintillator Monolithic scintillator based detector is another attractive approach. Compared to scintillator array-based detectors, the major advantages of
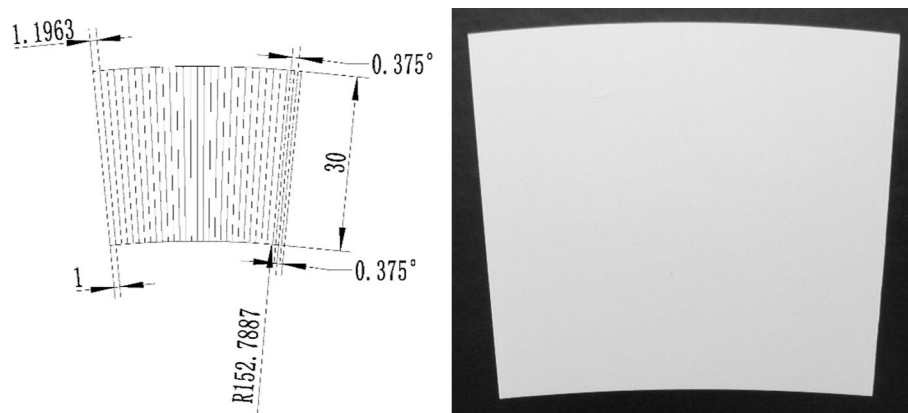
Fig. 7 (Left) Schematic and (right) photograph of a curved shape LYSO array used to minimize gaps between detector blocks [22]
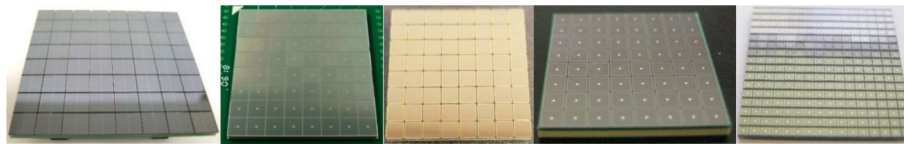

Fig. 8 SiPM arrays with different pixel sizes. (from left to right) 8 × 8 array of 6 × 6 mm^2 SiPMs from SensL, 8 × 8 array of 4 × 4 mm^2 SiPMs from Hamamatsu, 8 × 8 array of 3 × 3 mm^2 SiPMs from KETEK, 8 × 8 array of 2 × 2 mm^2 SiPMs from Hamamatsu, and 16 × 16 array of 1 × 1 mm^2 SiPMs from Hamamatsu [56, 128, 129, 139]

monolithic scintillator-based detectors are that the monolithic scintillator is easier to fabricate and the elimination of dead space due to reflector between detector elements—lending to potentially high sensitivity. The drawbacks are that more complicated position algorithms, such as deep learning or maximum likelihood method, are needed, and corrections for edge effects in the block are challenging [132, 133]. Different groups have been working on the optimization of the monolithic scintillator based detectors [132–136] and are showing improved performance. Several pre-clinical PET scanners based on monolithic detectors have been developed [28, 29, 134], which provides a way to scale up these scanners to total-body mouse/rat scanners. However, a tradeoff between spatial resolution and sensitivity is required and challenging to make. To obtain high sensitivity, 20–30 mm thick crystals are preferred. However, to obtain high spatial resolution with the monolithic scintillator, thin crystals are required. The β-CUBE PET scanner uses 8 mm thick LYSO, and the Albira Si PET scanner uses 10 mm-thick LYSO to obtain ∼ 1 mm spatial resolution and ∼ 10% sensitivity [28, 29]. It would be difficult to improve the positioning accuracy and hence spatial resolution without sacrificing the sensitivity, and vice versa.

Photodetector
Earlier PET scanners used PMTs as photodetectors; however, most state-of-the-art PET scanners currently use SiPMs as the photodetector [19, 31, 127, 137]. SiPMs and PMTs have similar gains of around 10^6. Compared to PMT, the advantages of SiPMs are their low working bias voltage (lower than 100 V), low noise, good single-photon
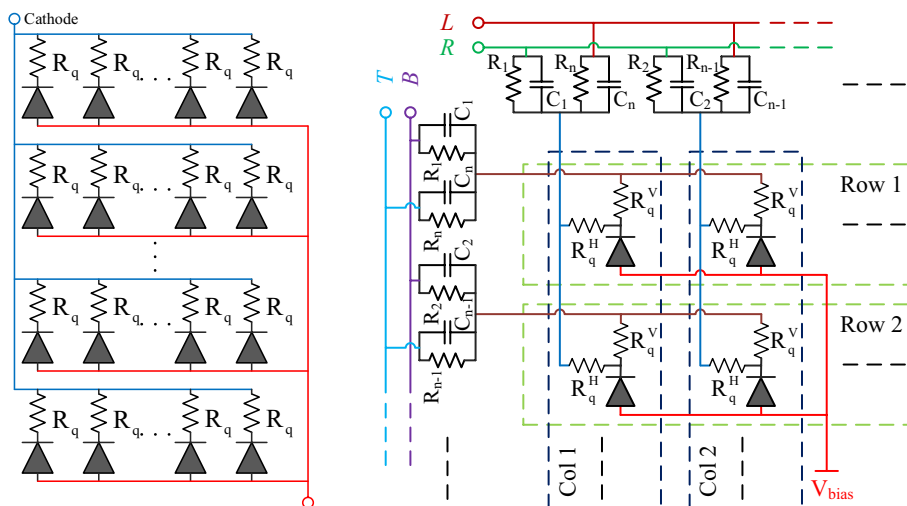
Fig. 9 Schematics of (left) non-PS-SiPM and (right) linearly-graded SiPM (LG-SiPM). LG-SiPM is a type of PS-SiPM [52]
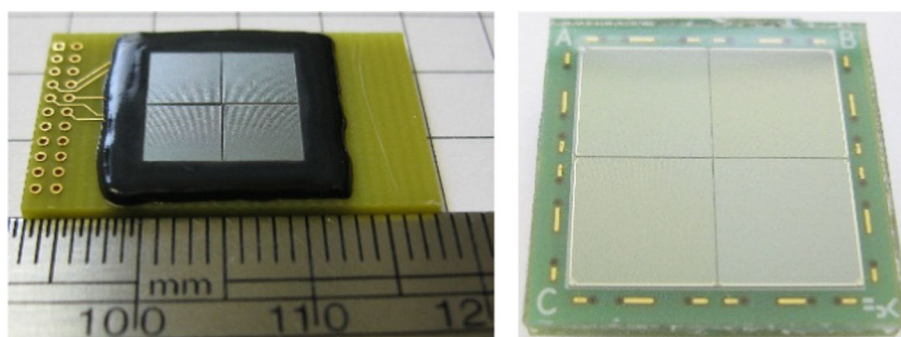

Fig. 10 Photographs of 2 × 2 PS-SiPM arrays from (left) Radiation Monitoring Devices, Inc. (RMD) [140, 143] and (right) Fondazione Bruno Kessler (FBK) [52]

timing resolution, compact size, and insensitive to magnetic fields [137]. Each SiPM pixel, consisting of hundreds to tens of thousands of microcells with sizes ranging from 5 to 100 um [138], can be fabricated in arrays of different sizes (Fig. 8) [56, 104, 128, 129, 139]. These SiPM arrays can be fabricated by arranging multiple SiPM pixels on various printed circuit boards (PCBs).

SiPMs are semiconductor devices that can be fabricated in most semiconductor foundries. Compared to PMT, the fabrication of SiPMs is much easier, which also leads to a lower cost. At this time, more than ten companies are involved in developing SiPMs. The performance of SiPMs has changed rapidly during the past 10 years resulting in mature products. Today, a range of high-performance SiPMs are provided by different companies (Figs. 8, 9). SiPM has been accepted as the standard photodetector by the PET community and revolutionized PET technology [137].

To develop SiPM for super-high-resolution PET applications, PS-SiPMs were invented (Figs. 9, 10) [52, 140–142]. For non-PS-SiPM (as these shown in Fig. 8), the anodes and cathodes of all the microcells in one SiPM pixel are connected to form one common anode and one common cathode (Fig. 9). In this way, the fired microcells of the SiPM

pixel cannot be located. To encode each microcell, a position encoding circuit for each microcell can be intergraded inside the SiPM. Different types of PS-SiPMs have been developed, and LYSO arrays with a 0.5 mm pitch size and 20 mm thickness have been clearly resolved [52]. Using PS-SiPM, small animal PET scanners with approaching the physically limited spatial resolution can be developed [12].

One critical disadvantage of the SiPM, compared to PMT, is the greater temperature dependency of the SiPM. Both the breakdown voltage and noise of SiPM change with the temperature. The lower the temperature, the lower the noise and the breakdown voltage. However, the animals are typically scanned under anesthesia and require heated beds to preserve physiological functions. To maintain the gain and keep the noise at an acceptable level, cooling, either using water or air, to minimize the temperature variation is necessary.

Readout electronics
As SiPMs are accepted as the standard photodetectors by the PET community and are widely used in different PET scanners, a range of application-specific integrated circuits (ASICs) or data acquisition systems (DAQs) have been developed for SiPM based PET scanners by different research groups or companies [144]. Examples for ASICs are the PETsys TOFPET ASIC [145], the HRFlexToT ASIC [146], and the PETA4 ASIC [147]. Companies like PETsys Electronics and Hamamatsu also provide complete data acquisition system solutions based on their ASICs for PET scanners [148, 149].

ASIC-based data acquisition systems have the advantages of low power and compact size; however, they are not flexible. To design flexible readouts for developing early prototype PET scanners, field-programmable gate array (FPGA)-based readouts, such as the FPGA-based Sigma-Delta analog-to-digital converter (ADC) readout system [150, 151] and FPGA-based comparators and time-to-digital converter (TDC) have been developed [152].

All these advances in readout electronics can be used for the development of total-body small animal PET scanners.

Challenges
Spatial resolution
Spatial resolution determines the finest anatomical structure that the scanner can resolve and still provide quantitative accuracy needed for measuring tissue concentration of its tracer concentration as limited by the partial volume effect. The lengths of most human bodies range from 150 cm to over 180 cm [153], while most of the laboratory used mice and rats have nose-to-anus-lengths smaller than 10 cm and 20 cm, respectively. The human brain has a linear diameter of ~ 11.0 cm, while the linear dimensions for mouse and rat are ~ 12 mm and ~ 8 mm (Fig. 11), respectively. Currently, clinical PET scanners have spatial resolutions as good as ~ 3.0 mm [19, 91], and dedicated human brain PET scanners with ~ 1-mm spatial resolutions are under development [95]. To obtain the same quantitative accuracy in mouse/rat studies as in human studies, PET scanners for total-body mouse and rat studies should have resolution better than 0.2 mm
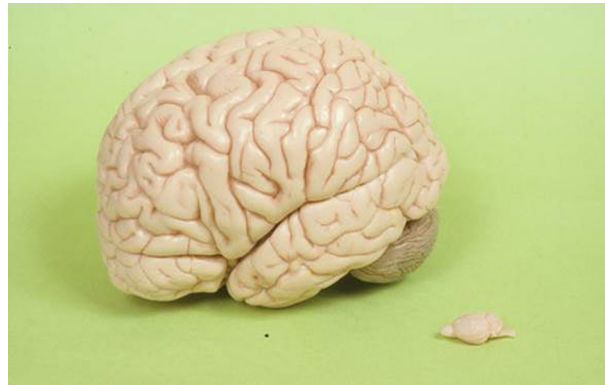
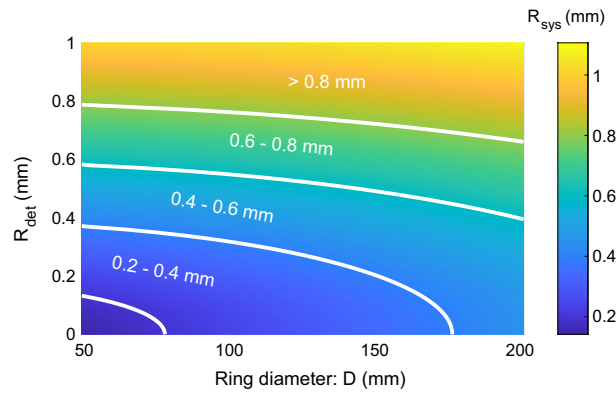**Fig. 11** Comparison of a human brain and a rat brain

Fig. 12 Fundamental spatial resolution versus ring diameter and detector resolution, assuming a 0.102 mm FWHM positron annihilation point distribution from the ^{18}F label source [155]. The resolutions are worse for larger ring diameters, which is caused by the noncollinearity of the annihilation photons as shown in formula (1) [18]

and 0.4 mm, respectively; for mouse/rat brain studies, the scanners should have resolution better than 0.1 mm. However, this is far beyond the spatial resolution of currently available small animal PET scanners (Fig. 2) [10–12].

The fundamental resolution of the PET scanner (R_{sys}) is determined by the detector resolution (R_{det}), the positron range (R_{range}), and the diameter of the scanner (D) [18, 154], which can be estimated using formula

$$R_{sys} = \sqrt{R_{det}^2 + R_{range}^2 + (0.0022D)^2} \tag{1}$$

where $0.0022D$ is caused by the noncollinearity of annihilation photons. To obtain higher system resolution, PET scanners need to have smaller ring diameters and use higher spatial resolution detectors.

For ^{18}F, which is the most widely used radionuclide today for labeling PET tracer molecules, the full width at half maximum (FWHM) of the positron annihilation point distribution is 0.102 mm (R_{range}) [155]. Then, the fundamental resolution of the scanner versus the detector resolution (R_{det}) and ring diameter (D) is shown in Fig. 12. It is obvious that it is impossible to achieve 0.1 mm spatial resolution, unless we will find radionuclides with

much smaller positron ranges in the future. The ring diameter can be reduced; however, it needs to be large enough to fit the animals into the scanner. A smaller diameter will also cause a larger parallax error (DOI effect). Hence, most of the PET research focuses on developing high-resolution PET detectors to improve the system-level resolution [52, 70, 107, 134, 156]. The most successful high resolution detectors which have been used at the scanner level were designed using scintillator arrays with ∼0.5 mm pitch size [69, 70]. However, further reducing the pitch size will reduce the detection efficiency of the detector through reducing the active area of the individual detector elements [12]. The loss of spatial positioning due to the photon scattering within the detector block will be larger for scintillator arrays with smaller pitch sizes, too. For monolithic crystal-based detectors, to obtain higher detector resolution, thinner crystals are required, which reduces the detection efficiency.

Depth-of-interaction information

To provide sufficient stopping power for the incoming gamma photon, detectors based on scintillator arrays or semiconductors need enough thickness, which causes the well-known parallax error, both in the radial direction and the axial direction (Fig. 13). The parallax error results in the resolution deteriorating as one moves away from the center of the scanner [25, 70]. To reduce the effect of parallax error, DOI information of the gamma photon interaction positions is needed [25]. In effect, to obtain uniform high resolution across the FOV, the DOI resolution needs to be at least as good as the detector resolution. Different methods have been proposed to obtain the DOI resolution [11, 157]. These include using monolithic scintillator [136, 158], multilayer scintillator [105, 159–163], customized reflector designs [116, 164, 165], and the dual-ended readout method [22, 22, 56, 166]. While current detectors based on scintillator arrays can have a resolution as good as 0.5 mm [52, 53, 156], it is still difficult to obtain the equivalent 0.5 mm DOI resolution without sacrificing other performance such as by reducing the thickness of the scintillator or significantly increasing the complexity of the detector. The best DOI resolution of 0.77 mm has been reported using the X'tal cube by segmenting the scintillator to $0.77 \times 0.77 \times 0.77$ mm^3 elements and reading out from six sides of the
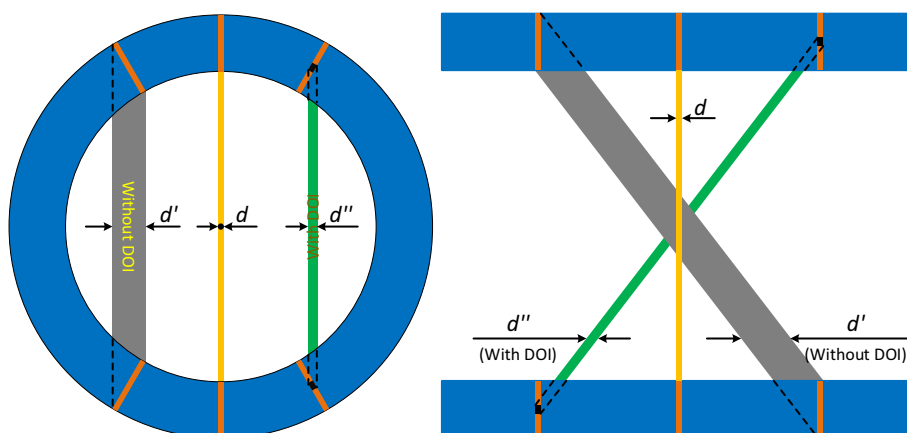

Fig. 13 Illustrates how the depth of interaction parallax effect deteriorates spatial resolution. The resolution of the scanner can be improved both in the radial direction and axial direction by obtaining DOI information. d is the width of the detector element in the scintillator array

scintillator block [163]. However, the complexity and cost of this detector are high, and the dead space between detector modules and hence sensitivity loss will be large if these detectors were to be used to build scanners.

Good DOI resolution is needed to obtain the best spatial resolution using thick scintillators. DOI resolutions of ~2 mm have been reported for 20 mm thick LYSO detectors [65], and ~1.2 mm DOI resolutions were obtained from 20 mm thick GAGG scintillators [167]. To date, the best achieved spatial resolution is ~0.5 mm using an LYSO array-based detector [52, 69, 70]. Hence, further significant effort is needed to improve the DOI resolution.

Timing resolution

Time-of-flight (TOF) information can be used to improve the effective sensitivity of PET by a factor of $\frac{L}{1.6c\delta_t}$, where δ_t is the timing resolution, L is the size of the animal, and c is the light speed [168–171]. Better timing resolution also can reduce the random coincidence event rate by using a narrower timing window [18], and maybe more interesting for direct positron emission imaging that eliminates the tomographic reconstruction, which introduces statistical noise [172]. However, the best timing resolution currently obtained using 20 mm thick L(Y)SO is ~100 ps [173]. For this, a pair of LSO detector elements with a size of $2 \times 2 \times 20$ mm^3 were used and read out using an oscilloscope with a bandwidth in GHz and a sampling rate of over giga-samples per second (GSPS). The timing resolution will be worse when the crystal cross-section area becomes smaller. This is because as within smaller crystals, the scintillation photons have more reflections, which causes more scintillation photon loss, before reaching the photodetectors, due to the increased reflection numbers on the four lateral sides of the crystal. At the moment, most of the small animal PET scanners still have a timing resolution in several nano-seconds [28, 30, 31], which is not useful for time-of-flight PET. Even 100 ps timing resolution, which corresponds to 3 cm in the distance, is not good enough for small animal PET studies. Improving the timing resolution of high-resolution small animal PET, such as good as 10 ps, to be as equivalent to what has been achieved for human PET scanners in increasing signal to noise is still a challenge and a long-term goal. Even when we have a 10 ps timing resolution, we still need image reconstruction for small animal PET scanners, as 10 ps timing resolution corresponds to 1.5 mm spatial resolution, which is not as good as current small animal PET scanners.

Inter-detector and inter-crystal scatter

Compton scatter, which causes inter-detector scatter and inter-crystal scatter in PET, is an unfavorable type of photon interaction. The inter-detector scatter happens when one gamma photon interacts with multiple detectors, which results in a loss of sensitivity or multiple coincidences (reducing image quality) [174–176]. The inter-crystal scatter happens when one gamma photon deposits its energy in multiple crystal elements within one detector. This deteriorates the spatial resolution, and hence image quality. [176–178]. The ratios of inter-detector scatter and inter-crystal scatter can be reduced using scintillators with higher density where the higher effective atomic number reduces the Compton scatter probability. However, none of the currently available scintillators has a negligible Compton scatter probability. The Compton scatter probability of L(Y)SO is 68%, and 60% for BGO [123]. The inter-detector scatter ratio also depends on the size of the detector module, where the larger the detector, the lower ratio of the

inter-detector scatter. The inter-crystal scatter ratio also depends on the cross-section size of the crystal elements. The smaller the crystal, the higher ratio of the inter-crystal scatter. Hence, for high resolution small animal PET scanners, especially those based on scintillator arrays with small pitch sizes, inter-detector scatter recovery and inter-crystal scatter recovery are both required to improve the sensitivity and resolution, respectively.

Different algorithms have been proposed for inter-detector scatter recovery and inter-crystal scatter recovery [171, 179–181]. However, it is still challenging to do it, especially for high-resolution PET scanners. High-resolution detectors always use light-sharing or charge-sharing methods to improve the spatial resolution and center-of-gravity method to calculate the interaction position [52, 104, 128]. The presence of inter-crystal scatter causes the crystal positioned by the center-of-gravity method is likely to be different from the initial interacted crystal.

Most of the currently available small animal scanners do not implement inter-detector and inter-crystal scatter recovery [28–31]. However, these are needed in order to approach the physically limited spatial resolution and to achieve maximum sensitivity.

Image reconstruction method

Total-body small animal PET scanners with high spatial resolution have a large number of crystal elements. This is true for both crystal array-based scanners and virtual crystal elements in monolithic crystal-based scanners. For example, the H^2RS160 PET and UHS-PET scanners consist of 460,800 and 115,200 crystal elements, respectively [12]. If 10-layer DOI information was used, those two scanners would effectively have 4,608,000 and 1,152,000 virtual crystal elements, respectively. Note this is considerably greater than the 2-meter axial long total-body EXPLORER PET scanner with 564,480 crystal elements [19, 182] but with no depth of interaction readout. Hence, highly efficient image reconstruction methods are needed to handle the billions of line-of-responses (LORs). Furthermore, to fully capitalize on the high spatial resolution of a PET scanner, which has optimal geometry for data collection, corrections for the positron range [183, 184] and the inter-crystal scatter should be modeled precisely. In turn, they need to be included in the image reconstructions, which represent ongoing challenges that will require much further effort.

Scintillator

Although L(Y)SO scintillators have been widely adopted by most of the PET scanners, a major drawback of them is the intrinsic radiation emitted from the ^{176}Lu. This radionuclide decays with β^- emission into ^{176}Hf, together with a cascade of 307 keV, 202 keV, and 88 keV γ photons which are emitted in coincidence [185]. The estimated activity of ^{176}Lu in L(Y)SO, is about 240–300 Bq/cm^{-3}, which limits the performance of PET scanners based on L(Y)SO for low-dose studies, including cell tracking and gene expression research [11, 60, 61, 64]. As the case for most clinical PET scanners, the lower level of the coincident energy window is set above 350 keV to reduce the effect of the background radiation [122]. However, (1) in small animal PET studies, especially in mouse studies, a threshold lower than 350 keV is preferred to achieve high sensitivity, and (2) even using a tight energy window such as 350–650 keV, the summed energy of the cascade γ photons still can fall into the energy window and degrades the PET image quality. How to optimize the energy window of L(Y)SO-based PET scanners for different applications is a challenging task and needs to be systematically addressed.

Other crystals, such as the recently developed gadolinium aluminum gallium garnet (GAGG) scintillator has a higher light yield than L(Y)SO scintillator [156]. However, GAGG has a lower density, lower stopping power, and slower decay time.

Electronics

Compared to scanners based on detectors without DOI capabilities, scanners with DOI capabilities require more complex readout electronics to record and process the DOI information. One example is the dual-ended readout detector, which requires 2 times photodetectors. Hence, signal-multiplexing readouts are always used to reduce the electronic channels that need to be digitized [65, 143]. Total-body small animal PET scanners will also produce a large amount of data. The electronics needs to have the ability to acquire and store the data online and reconstruct the images quickly. On the acquisition and storage side, the dead time of the readout electronics needs to be as small as possible, especially when the scanner is used for high count rate dynamic studies to measure the time-activity curves (TACs) from the reconstructed images. On the reconstruction side, total-body small animal PET scanner with DOI information will have a large number of LORs. For a dual-ended readout detector or monolithic crystal-based scanner, the number of possible LORs would be infinite if continuous DOI information is used, which makes it challenging to generate a sensitivity map [186] and increases the required storage and/or memory size. A practical way is to use discrete DOI information based on the discrete DOI resolution. Taken the H^{2}RS110 PET as an example, it has 204,800 crystals [12]. The DOI resolution of the detectors is $\sim$2 mm. In our simulation, each crystal is divided into 10 virtual crystals with 2 mm thickness in the radial direction. With using this discrete DOI information, the scanner has 2,048,000 virtual crystals with billions of possible LORs, which is still much more than the human total-body EXPLORER PET with 564,480 crystals [19]. Hence, high efficiency image reconstruction methods that can reduce the image reconstruction time and computational load are required, both for crystal array and monolithic crystal-based scanners. However, given the computing power of today's graphics processing units (GPU) and central processing units (CPU), if economic costs are not a consideration, undertaking the necessary electronic processing is well within the capability of existing technology.

Mechanical design

One of the goals to design total-body small animal PET scanners is to improve the sensitivity. Hence, detector modules need to be packed tightly to minimize the gap/dead space between detector modules in both axial and transaxial directions to improve the sensitivity. At the same time, the temperature of the detector, especially for temperature-sensitive photodetectors such as SiPM, needs to be controlled.

Conclusions

The development and construction of small animal PET scanners has established roles in biomedical engineering. The technology has advanced considerably since the reporting of the early systems [9, 187]. However, none of the currently available small animal scanners have both high enough sensitivity to approach the physically limited spatial resolution. However, it is obvious that quantitative accuracy and quantitative precision can be improved by using scanners with identified means for realizing higher spatial resolution and sensitivity. As a

result of the efforts from groups in different research fields, it is now possible to increase the performance of small animal PET scanners that promise to open up new application areas of molecular imaging in small laboratory animals. One obvious way to improve the sensitivity to image the whole animal is to build total-body scanners with longer axial lengths than that of the animals. The technologies to enable this are in place, although there are still challenges, such as how to improve the DOI resolution to reduce parallax error and correct for inter-crystal scatter. Dual-ended readout detectors based on PS-SiPM and scintillator arrays are expected to be the most promising candidates for building total-body small animal PET scanners that could approach the theoretically achievable resolution and high sensitivity. We project that the reported under-construction scanner (the HS-BGO PET and H2RS110 PET shown in Figs. 1, 2) with significantly improved sensitivity will open new applications using small animal PET and thereby lead the way to the further development of total-body small animal PET scanners. However, many technical questions and challenges still need to be addressed as have been discussed in this article. However, we suspect many technical opportunities and challenges remain to be uncovered. We look forward to researchers from PET communities, both in the academia and industry, to resolve these challenges to develop the next generations of small animal PET scanners with improved performance, and thereby enhance molecular imaging based research in small laboratory animals.

Appendix

See Table 3.

Table 3 Abbreviations of PET scanners shown in Figs. 1, 2, 3, and 4

Abbreviation	Description	References
NanoPET	Commercially available scanner provided by Mediso	[45]
A-PET	An animal PET scanner developed by Dr. Suleman Surti	[40]
Inveon	Siemens Inveon PET	[43]
Metis	Metis PET is commercially provided by Shandong Madic Technology Co.,Ltd	[47]
IRIS	IRIS PET is commercially provided by Medilumine Inc	[46]
ClairvivoPET	ClairvivoPET is a commercial provided by Shimadzu Corp., Japan	[41]
HiPET	A small animal PET scanner developed by Dr. Zheng Gu	[30]
LabPET-12	Scanner developed at University de Sherbrooke, Canada	[42]
ClearPET	ClearPET was manufactured by Raytest Isotopenmessgeraete GmbH, Germany	[44]
Albira Si PET	Bruker Albira Si fully integrated PET/SPECT/CT	[29]
SIAT aPET	A small animal PET developed at Shenzhen Institute of Advanced Technology, China	[31]
β-CUBE	Scanner developed by MOLECUBES, Belgium	[28]
quadHIDAC32	Scanner developed by Oxford Positron Systems	[38]
SimPET-X	A PET insert for simultaneous mouse total-body PET/MR imaging	[13]
Yamaya's PET	A total-body small animal PET is underdeveloped at Dr. Taiga Yamaya's Lab, Japan	[21]
Mouse J-PET	A total-body mouse J-PET simulated by Jagiellonian University	[48]
Rat J-PET	A total-body rat J-PET simulated by Jagiellonian University	[48]
HS-BGO PET	A total-body small animal PET with ~330-mm axial FOV is underdeveloped at University of California at Davis	[49]
H^2RS110	A high-resolution (0.5 mm) and high sensitivity PET with 167-mm axial FOV is underdeveloped at University of California at Davis	[12]
H^2RS160	A high-resolution (0.5 mm) and high sensitivity PET with 254-mm axial FOV simulated at University of California at Davis	[12]
UHS-PET	An over 50% sensitivity PET proposed and simulated by University of California at Davis	[50]

Abbreviations

ADC	Analog-to-digital converter
ASIC	Application-specific integrated circuit
BGO	Bismuth germanate
CPU	Central processing unit
DAQ	Data acquisition system
DOI	Depth-of-interaction
EW	Energy window
FBK	Fondazione Bruno Kessler
FBP	Filtered back projection
FDG	Fluorodeoxyglucose
FOV	Field-of-view
FPGA	Field-programmable gate array
FWHM	Full width at half maximum
GAGG	Gadolinium aluminum gallium garnet
GPU	Graphics processing unit
GSOZ	Zr-doped gadolinium oxyorthosilicate
GSPS	Giga-samples per second
IDIF	Image-derived input function
LG-SiPM	Linearly graded SiPM
LOR	Line-of-response
LYSO	Lutetium–yttrium oxyorthosilicate
MAPMT	Multi-anode photomultiplier tube
ML	Maximum likelihood
MLEM	Maximum likelihood expectation maximization
MRPC	Multigap resistive plate chamber
MWPC	Multiwire proportional chamber
OSEM	Ordered subset expectation maximization
PCB	Printed circuit board
PET	Positron emission tomography
PMT	Photomultiplier tube
PS-SiPM	Position-sensitive SiPM
PVE	Partial volume effect
RMD	Radiation Monitoring Devices, Inc.
SiPM	Silicon photomultiplier
SNR	Signal-to-noise ratio
SUV	Standard uptake value
TAC	Time-activity curve
TDC	Time-to-digital converter
TOF	Time-of-flight
TSPO	Translocator protein

Availability of data and materials
Not applicable.

Code availability
Not applicable.

Declarations

Ethics approval and consent to participate
Not applicable.

Consent for publication
Not applicable.

Competing interests
No potential conflicts of interest relevant to this article exist.

References

1. Malakoff D. The rise of the mouse, biomedicine's model mammal. Science. 2000;288:248–53.
2. Zhao S, Shetty J, Hou L, Delcher A, Zhu B, Osoegawa K, et al. Human, mouse, and rat genome large-scale rearrangements: stability versus speciation. Genome Res. 2004;14:1851–60.
3. Cherry SR. The 2006 Henry N. Wagner lecture: of mice and men (and positrons)—advances in PET imaging technology. J Nucl Med. 2006;47:1735–45.
4. Taylor K, Gordon N, Langley G, Higgins W. Estimates for worldwide laboratory animal Use in 2005. Altern Lab Anim. 2008;36:327–42.
5. de Kemp RA, Epstein FH, Catana C, Tsui BMW, Ritman EL. Small-animal molecular imaging methods. J Nucl Med. 2010;51:18S-32S.
6. Toyohara J, Ishiwata K. Animal tumor models for PET in drug development. Ann Nucl Med. 2011;25:717–31.
7. Cuccurullo V, Di Stasio GD, Schillirò ML, Mansi L. Small-animal molecular imaging for preclinical cancer research: μPET and μSPECT. Curr Radiopharm. 2016;9:102–13.
8. Carbone L. Estimating mouse and rat use in American laboratories by extrapolation from Animal Welfare Act-regulated species. Sci Rep. 2021;11:493.
9. Cherry SR, Shao Y, Silverman RW, Meadors K, Siegel S, Chatziioannou A, et al. MicroPET: a high resolution PET scanner for imaging small animals. IEEE Trans Nucl Sci. 1997;44:1161–6.
10. Miyaoka RS, Lehnert AL. Small animal PET: a review of what we have done and where we are going. Phys Med Biol. 2020;65:24TR04.
11. Amirrashedi M, Zaidi H, Ay MR. Advances in preclinical PET instrumentation. PET Clin. 2020;15:403–26.
12. Lai Y, Wang Q, Zhou S, Xie Z, Qi J, Cherry SR, et al. H2RSPET: a 0.5 mm resolution high-sensitivity small-animal PET scanner, a simulation study. Phys Med Biol. 2021;66:065016.
13. Kim KY, Son J-W, Kim K, Chung Y, Park JY, Lee Y-S, et al. Performance evaluation of SimPET-X, a PET insert for simultaneous mouse total-body PET/MR imaging. Mol Imaging Biol. 2021;23:703–13.
14. Jones T. Total body PET imaging from mice to humans. Front Phys. 2020. https://doi.org/10.3389/fphy.2020.00077.
15. Surti S, Pantel AR, Karp JS. Total body PET: why, how, what for? IEEE Trans Radiat Plasma Med Sci. 2020;4:283–92.
16. Saboury B, Morris MA, Farhadi F, Nikpanah M, Werner TJ, Jones EC, et al. Reinventing molecular imaging with total-body PET, part I: technical revolution in evolution. PET Clin. 2020;15:427–38.
17. Surti S, Guerra AD, Zaidi H. Total-body PET is ready for prime time. Med Phys. 2021;48:3–6.
18. Cherry SR, Sorenson JA, Phelps ME. Physics in nuclear medicine E-book. Amsterdam: Elsevier; 2012.
19. Cherry SR, Jones T, Karp JS, Qi J, Moses WW, Badawi RD. Total-body PET: maximizing sensitivity to create new opportunities for clinical research and patient care. J Nucl Med. 2018;59:3–12.
20. Zhang X, Cherry SR, Xie Z, Shi H, Badawi RD, Qi J. Subsecond total-body imaging using ultrasensitive positron emission tomography. PNAS Natl Acad Sci. 2020;117:2265–7.
21. Kang HG, Tashima H, Yoshida E, Higuchi M, Yamaya T. A total-body small animal PET scanner with a 4-layer DOI detector. J Nucl Med. 2021;62:1148–1148.
22. Du J, Bai X, Liu C-C, Qi J, Cherry SR. Design and evaluation of gapless curved scintillator arrays for simultaneous high-resolution and high-sensitivity brain PET. Phys Med Biol. 2019;64:235004.
23. Zhang X, Xie Q, Xie S, Yu X, Xu J, Peng Q. A novel portable gamma radiation sensor based on a monolithic lutetium–yttrium oxyorthosilicate ring. Sensors. 2021;21:3376.
24. Stolin AV, Martone PF, Jaliparthi G, Raylman RR. Preclinical positron emission tomography scanner based on a monolithic annulus of scintillator: initial design study. JMI. 2017;4:011007.
25. Yoshida E, Tashima H, Hirano Y, Inadama N, Nishikido F, Murayama H, et al. Spatial resolution limits for the isotropic-3D PET detector X'tal cube. Nucl Instrum Methods Phys Res Sect A. 2013;728:107–11.
26. Lin S-Y, Craythorn RG, O'Connor AE, Matzuk MM, Girling JE, Morrison JR, et al. Female infertility and disrupted angiogenesis are actions of specific follistatin isoforms. Mol Endocrinol. 2008;22:415–29.
27. Schellong K, Neumann U, Rancourt RC, Plagemann A. Increase of long-term 'diabesity' risk, hyperphagia, and altered hypothalamic neuropeptide expression in neonatally overnourished 'small-for-gestational-age' (SGA) rats. PLoS ONE. 2013;8:e78799.
28. Krishnamoorthy S, Blankemeyer E, Mollet P, Surti S, Holen RV, Karp JS. Performance evaluation of the MOLECUBES β-CUBE—a high spatial resolution and high sensitivity small animal PET scanner utilizing monolithic LYSO scintillation detectors. Phys Med Biol. 2018;63:155013.
29. Gsell W, Molinos C, Correcher C, Belderbos S, Wouters J, Junge S, et al. Characterization of a preclinical PET insert in a 7 tesla MRI scanner: beyond NEMA testing. Phys Med Biol. 2020;65:245016.
30. Gu Z, Taschereau R, Vu NT, Prout DL, Lee J, Chatziioannou AF. Performance evaluation of HiPET, a high sensitivity and high resolution preclinical PET tomograph. Phys Med Biol. 2020;65:045009.
31. Kuang Z, Wang X, Ren N, Wu S, Gao J, Zeng T, et al. Design and performance of SIAT aPET: a uniform high-resolution small animal PET scanner using dual-ended readout detectors. Phys Med Biol. 2020;65:235013.
32. Dedeurwaerdere S, Callaghan PD, Pham T, Rahardjo GL, Amhaoul H, Berghofer P, et al. PET imaging of brain inflammation during early epileptogenesis in a rat model of temporal lobe epilepsy. EJNMMI Res. 2012;2:60.
33. Becker G, Warnier C, Serrano ME, Bahri MA, Mercier J, Lemaire C, et al. Pharmacokinetic characterization of [18F] UCB-H PET radiopharmaceutical in the rat brain. Mol Pharm. 2017;14:2719–25.
34. Sinharay S, Tu T-W, Kovacs ZI, Schreiber-Stainthorp W, Sundby M, Zhang X, et al. In vivo imaging of sterile microglial activation in rat brain after disrupting the blood-brain barrier with pulsed focused ultrasound: [18F]DPA-714 PET study. J Neuroinflamm. 2019;16:155.
35. Toyonaga T, Smith LM, Finnema SJ, Gallezot J-D, Naganawa M, Bini J, et al. In vivo synaptic density imaging with 11C-UCB-J detects treatment effects of saracatinib in a mouse model of alzheimer disease. J Nucl Med. 2019;60:1780–6.
36. Sadasivam P, Fang XT, Toyonaga T, Lee S, Xu Y, Zheng M-Q, et al. Quantification of SV2A binding in rodent brain using [18F]SynVesT-1 and PET imaging. Mol Imaging Biol. 2021;23:372–81.

37. Missimer J, Madi Z, Honer M, Keller C, Schubiger A, Ametamey S-M. Performance evaluation of the 16-module quad-HIDAC small animal PET camera. Phys Med Biol. 2004;49:2069–81.

38. Schäfers KP, Reader AJ, Kriens M, Knoess C, Schober O, Schäfers M. Performance evaluation of the 32-Module quadHIDAC small-animal PET scanner. J Nucl Med. 2005;46:996–1004.

39. Hastings DL, Reader AJ, Julyan PJ, Zweit J, Jeavons AP, Jones T. Performance characteristics of a small animal PET camera for molecular imaging. Nucl Instrum Methods Phys Res Sect A. 2007;573:80–3.

40. Surti S, Karp JS, Perkins AE, Cardi CA, Daube-Witherspoon ME, Kuhn A, et al. Imaging performance of a-PET: a small animal PET camera. IEEE Trans Med Imaging. 2005;24:844–52.

41. Sato K, Shidahara M, Watabe H, Watanuki S, Ishikawa Y, Arakawa Y, et al. Performance evaluation of the small-animal PET scanner ClairvivoPET using NEMA NU 4-2008 Standards. Phys Med Biol. 2015;61:696–711.

42. Bergeron M, Cadorette J, Tétrault M-A, Beaudoin J-F, Leroux J-D, Fontaine R, et al. Imaging performance of LabPET APD-based digital PET scanners for pre-clinical research. Phys Med Biol. 2014;59:661–78.

43. Bao Q, Newport D, Chen M, Stout DB, Chatziioannou AF. Performance evaluation of the inveon dedicated PET preclinical tomograph based on the NEMA NU-4 standards. J Nucl Med. 2009;50:401–8.

44. Cañadas M, Embid M, Lage E, Desco M, Vaquero JJ, Pérez JM. NEMA NU 4-2008 performance measurements of two commercial small-animal PET scanners: ClearPET and rPET-1. IEEE Trans Nucl Sci. 2011;58:58–65.

45. Szanda I, Mackewn J, Patay G, Major P, Sunassee K, Mullen GE, et al. National Electrical Manufacturers Association NU-4 performance evaluation of the PET component of the NanoPET/CT preclinical PET/CT scanner. J Nucl Med. 2011;52:1741–7.

46. Belcari N, Camarlinghi N, Ferretti S, Iozzo P, Panetta D, Salvadori PA, et al. NEMA NU-4 performance evaluation of the IRIS PET/CT preclinical scanner. IEEE Trans Radiat Plasma Med Sci. 2017;1:301–9.

47. Liu Q, Li C, Liu J, Krish K, Fu X, Zhao J, et al. Technical note: performance evaluation of a small-animal PET/CT system based on NEMA NU 4-2008 standards. Med Phys. 2021;48:5272–82.

48. Dadgar M, Parzych S, Tayefi Ardebili F, Baran J, Chug N, Curceanu C, et al. Investigation of novel preclinical Total Body PET designed with J-PET technology: a simulation study. IEEE Trans Radiat Plasma Med Sci. 2022. https://doi.org/10.1109/TRPMS.2022.3211780.

49. Wang Q, Cherry S, Du J. Design of a high sensitivity total-body small animal BGO PET scanner for low activity imaging: a simulation study. Manchester, UK; 2019.

50. Liu C-C, Du J, Wang Q, Cherry S, Qi J. High spatial resolution and sensitivity total body preclinical PET based on gapless curved crystal arrays and dual-ended readouts: a simulation study. Virtual; 2021.

51. Du J, Yang Y, Berg E, Bai X, Gola A, Ferri A, et al. Evaluation of linearly-graded SiPMs for high resolution small-animal PET. Biomed Phys Eng Express. 2015;1:045008.

52. Du J, Bai X, Gola A, Acerbi F, Ferri A, Piemonte C, et al. Performance of a high-resolution depth-encoding PET detector module using linearly-graded SiPM arrays. Phys Med Biol. 2018;63:035035.

53. Kuang Z, Wang X, Fu X, Ren N, Yang Q, Zhao B, et al. Dual-ended readout small animal PET detector by using 0.5 mm pixelated LYSO crystal arrays and SiPMs. Nucl Instrum Methods Phys Res Sect A Accel Spectrom Detect Assoc Equip. 2019;917:1–8.

54. Hirano Y, Nitta M, Inadama N, Nishikido F, Yoshida E, Murayama H, et al. Performance evaluation of a depth-of-interaction detector by use of position-sensitive PMT with a super-bialkali photocathode. Radiol Phys Technol. 2014;7:57–66.

55. Ahmed AM, Chacon A, Rutherford H, Akamatsu G, Mohammadi A, Nishikido F, et al. A validated Geant4 model of a whole-body PET scanner with four-layer DOI detectors. Phys Med Biol. 2020;65:235051.

56. Du J. Performance of dual-ended readout PET detectors based on BGO arrays and BaSO4 reflector. IEEE Trans Radiat Plasma Med Sci. 2021;6:1–1.

57. de Marcillac P, Coron N, Dambier G, Leblanc J, Moalic J-P. Experimental detection of α-particles from the radioactive decay of natural bismuth. Nature. 2003;422:876–8.

58. Lewellen TK. Recent developments in PET detector technology. Phys Med Biol. 2008;53:R287-317.

59. Du J, Wang Y, Zhang L, Zhou Z, Xu Z, Wang X. Physical properties of LYSO scintillator for NN-PET detectors. In: 2009 2nd international conference on biomedical engineering and informatics; 2009. p. 1–5.

60. van Dongen GAMS, Boellaard R, Vugts DJ. In vivo tracking of single cells with PET. Nat Biomed Eng. 2020;4:765–6.

61. Jung KO, Kim TJ, Yu JH, Rhee S, Zhao W, Ha B, et al. Whole-body tracking of single cells via positron emission tomography. Nat Biomed Eng. 2020;4:835–44.

62. Gambhir SS, Barrio JR, Phelps ME, Iyer M, Namavari M, Satyamurthy N, et al. Imaging adenoviral-directed reporter gene expression in living animals with positron emission tomography. PNAS Natl Acad Sci. 1999;96:2333–8.

63. Blasberg R. PET imaging of gene expression. Eur J Cancer. 2002;38:2137–46.

64. Sharma V, Luker GD, Piwnica-Worms D. Molecular imaging of gene expression and protein function in vivo with PET and SPECT. J Magn Reson Imaging. 2002;16:336–51.

65. Yang Q, Kuang Z, Sang Z, Yang Y, Du J. Performance comparison of two signal multiplexing readouts for SiPM-based pet detector. Phys Med Biol. 2019;64:23NT02.

66. Du J, Peng P, Bai X, Cherry SR. Shared-photodetector readout to improve the sensitivity of positron emission tomography. Phys Med Biol. 2018;63:205002.

67. Niedźwiecki S, Białas P, Curceanu C, Czerwiński E, Dulski K, Gajos A, et al. J-PET: a new technologyfor the whole-body PET imaging. Acta Phys Pol B. 2017;48:1567–76.

68. Kowalski P, Wiślicki W, Shopa RY, Raczyński L, Klimaszewski K, Curcenau C, et al. Estimating the NEMA characteristics of the J-PET tomograph using the GATE package. Phys Med Biol. 2018;63:165008.

69. Yang Y, Bec J, Zhou J, Zhang M, Judenhofer MS, Bai X, et al. A prototype high-resolution small-animal PET scanner dedicated to mouse brain imaging. J Nucl Med. 2016;57:1130–5.

70. Yamamoto S, Watabe H, Watabe T, Ikeda H, Kanai Y, Ogata Y, et al. Development of ultrahigh resolution Si-PM-based PET system using 0.32mm pixel scintillators. Nucl Instrum Methods Phys Res Sect A Accel Spectrom Detect Assoc Equip. 2016;836:7–12.

71. Zhang X, Xie Z, Berg E, Judenhofer MS, Liu W, Xu T, et al. Total-body dynamic reconstruction and parametric imaging on the uEXPLORER. J Nucl Med. 2020;61:285–91.
72. Karakatsanis NA, Lodge MA, Tahari AK, Zhou Y, Wahl RL, Rahmim A. Dynamic whole-body PET parametric imaging: I. Concept, acquisition protocol optimization and clinical application. Phys Med Biol. 2013;58:7391–418.
73. Rahmim A, Lodge MA, Karakatsanis NA, Panin VY, Zhou Y, McMillan A, et al. Dynamic whole-body PET imaging: principles, potentials and applications. Eur J Nucl Med Mol Imaging. 2019;46:501–18.
74. Hood L, Heath JR, Phelps ME, Lin B. Systems biology and new technologies enable predictive and preventative medicine. Science. 2004;306:640–3.
75. Hacker M, Hicks RJ, Beyer T. Applied systems biology—embracing molecular imaging for systemic medicine. Eur J Nucl Med Mol Imaging. 2020;47:2721–5.
76. Goorden MC, van der Have F, Kreuger R, Ramakers RM, Vastenhouw B, Burbach JPH, et al. VECTor: a preclinical imaging system for simultaneous submillimeter SPECT and PET. J Nucl Med. 2013;54:306–12.
77. Jagoda EM, Vaquero JJ, Seidel J, Green MV, Eckelman WC. Experiment assessment of mass effects in the rat: implications for small animal PET imaging. Nucl Med Biol. 2004;31:771–9.
78. Kung M-P, Kung HF. Mass effect of injected dose in small rodent imaging by SPECT and PET. Nucl Med Biol. 2005;32:673–8.
79. Lambrecht RM, Eckelman WC, Rescigno A. Animal models in biomedical research and radiotracer design. In: Lambrecht RM, Eckelman WC, editors. Animal models in radiotracer design. New York, NY: Springer; 1983. p. 1–34. https://doi.org/10.1007/978-1-4612-5596-3_1.
80. Kaneta T, Ogawa M, Motomura N, Iizuka H, Arisawa T, Hino-Shishikura A, et al. Initial evaluation of the Celesteion large-bore PET/CT scanner in accordance with the NEMA NU2-2012 standard and the Japanese guideline for oncology FDG PET/CT data acquisition protocol version 2.0. EJNMMI Res. 2017;7:83.
81. van Sluis J, de Jong J, Schaar J, Noordzij W, van Snick P, Dierckx R, et al. Performance characteristics of the digital biograph vision PET/CT system. J Nucl Med. 2019;60:1031–6.
82. Hsu DFC, Ilan E, Peterson WT, Uribe J, Lubberink M, Levin CS. Studies of a next-generation silicon-photomultiplier-based time-of-flight PET/CT system. J Nucl Med. 2017;58:1511–8.
83. Zhang J, Maniawski P, Knopp MV. Performance evaluation of the next generation solid-state digital photon counting PET/CT system. EJNMMI Res. 2018;8:97.
84. Tan H, Sui X, Yin H, Yu H, Gu Y, Chen S, et al. Total-body PET/CT using half-dose FDG and compared with conventional PET/CT using full-dose FDG in lung cancer. Eur J Nucl Med Mol Imaging. 2021;48:1966–75.
85. Zhao Y-M, Li Y-H, Chen T, Zhang W-G, Wang L-H, Feng J, et al. Image quality and lesion detectability in low-dose pediatric 18F-FDG scans using total-body PET/CT. Eur J Nucl Med Mol Imaging. 2021;48:3378–85.
86. Liu G, Hu P, Yu H, Tan H, Zhang Y, Yin H, et al. Ultra-low-activity total-body dynamic PET imaging allows equal performance to full-activity PET imaging for investigating kinetic metrics of 18F-FDG in healthy volunteers. Eur J Nucl Med Mol Imaging. 2021;48:2373–83.
87. Wimberley C, Lavisse S, Hillmer A, Hinz R, Turkheimer F, Zanotti-Fregonara P. Kinetic modeling and parameter estimation of TSPO PET imaging in the human brain. Eur J Nucl Med Mol Imaging. 2021;49:246–56.
88. Fairley LH, Sahara N, Aoki I, Ji B, Suhara T, Higuchi M, et al. Neuroprotective effect of mitochondrial translocator protein ligand in a mouse model of tauopathy. J Neuroinflamm. 2021;18:76.
89. Bertoglio D, Amhaoul H, Goossens J, Ali I, Jonckers E, Bijnens T, et al. TSPO PET upregulation predicts epileptic phenotype at disease onset independently from chronic TSPO expression in a rat model of temporal lobe epilepsy. NeuroImage Clin. 2021;31:102701.
90. Hume SP, Gunn RN, Jones T. Pharmacological constraints associated with positron emission tomographic scanning of small laboratory animals. Eur J Nucl Med. 1998;25:173–6.
91. Badawi RD, Shi H, Hu P, Chen S, Xu T, Price PM, et al. First human imaging studies with the EXPLORER total-body PET scanner*. J Nucl Med. 2019;60:299–303.
92. Daube-Witherspoon ME, Viswanath V, Werner ME, Karp JS. Performance characteristics of long axial field-of-view PET scanners with axial gaps. IEEE Trans Radiat Plasma Med Sci. 2021;5:322–30.
93. Prenosil GA, Hentschel M, Fürstner M, Sari H, Rominger A. NEMA NU 2-2018 performance measurements of Biograph Vision Quadra PET/CT system. Nuklearmedizin. 2021;60:152.
94. Moliner L, Rodríguez-Alvarez MJ, Catret JV, González A, Ilisie V, Benlloch JM. NEMA performance evaluation of CareMiBrain dedicated brain PET and comparison with the whole-body and dedicated brain PET systems. Sci Rep. 2019;9:15484.
95. Gaudin É, Toussaint M, Thibaudeau C, Paillé M, Fontaine R, Lecomte R. Performance simulation of an ultrahigh resolution brain PET scanner using 1.2-mm pixel detectors. IEEE Trans Radiat Plasma Med Sci. 2019;3:334–42.
96. Wang Z, Cao X, Zeng X, LaBella A, Petersen E, Clayton N, et al. A high resolution and high sensitivity Prism-PET brain scanner with non-cylindrical decagon geometry. J Nucl Med. 2021;62:1136–1136.
97. Carson R, Berg E, Badawi R, Cherry S, Du J, Feng T, et al. Design of the NeuroEXPLORER, a next-generation ultra-high performance human brain PET imager. J Nucl Med. 2021;62:1120–1120.
98. Lammertsma AA. Forward to the past: the case for quantitative PET imaging. J Nucl Med. 2017;58:1019–24.
99. Wang G, Rahmim A, Gunn RN. PET parametric imaging: past, present, and future. IEEE Trans Radiat Plasma Med Sci. 2020;4:663–75.
100. Wu Y, Feng T, Zhao Y, Xu T, Fu F, Huang Z, et al. Whole-body parametric imaging of FDG PET using uEXPLORER with reduced scan time. J Nucl Med. 2022;63:622–8.
101. Alf MF, Wyss MT, Buck A, Weber B, Schibli R, Krämer SD. Quantification of brain glucose metabolism by 18F-FDG PET with real-time arterial and image-derived input function in mice. J Nucl Med. 2013;54:132–8.
102. Colazzo F, Castiglioni L, Sironi L, Fontana L, Nobili E, Franzosi M, et al. Murine left atrium and left atrial appendage structure and function: echocardiographic and morphologic evaluation. PLoS ONE. 2015;10:e0125541.
103. Wei S, Joshi N, Salerno M, Ouellette D, Saleh L, De Lorenzo C, et al. PET imaging of leg arteries for determining the input function in PET/MRI brain studies using a compact, MRI-compatible PET system. IEEE Trans Radiat Plasma Med Sci. 2021;6:1–1.

104. Du J, Yang Y, Bai X, Judenhofer MS, Berg E, Di K, et al. Characterization of large-area SiPM array for PET applications. IEEE Trans Nucl Sci. 2016;63:8–16.

105. Watanabe M, Saito A, Isobe T, Ote K, Yamada R, Moriya T, et al. Performance evaluation of a high-resolution brain PET scanner using four-layer MPPC DOI detectors. Phys Med Biol. 2017;62:7148–66.

106. Beltrame P, Bolle E, Braem A, Casella C, Chesi E, Clinthorne N, et al. The AX-PET demonstrator—design, construction and characterization. Nucl Instrum Methods Phys Res Sect A. 2011;654:546–59.

107. Jin Y, Tanton P, Streicher M, Yang H, Brown S, He Z, et al. Experimental evaluation of a prototype combined PET-Compton imaging system based on 3-D position-sensitive CZT detectors for dedicated breast cancer imaging. J Nucl Med. 2021;62:1129–1129.

108. Ariño-Estrada G, Du J, Kim H, Cirignano LJ, Shah KS, Cherry SR, et al. Development of TlBr detectors for PET imaging. Phys Med Biol. 2018;63:13NT04.

109. Ishii K, Kikuchi Y, Matsuyama S, Kanai Y, Kotani K, Ito T, et al. First achievement of less than 1mm FWHM resolution in practical semiconductor animal PET scanner. Nucl Instrum Methods Phys Res Sect A. 2007;576:435–40.

110. Gallego Manzano L, Abaline JM, Acounis S, Beaupère N, Beney JL, Bert J, et al. XEMIS2: a liquid xenon detector for small animal medical imaging. Nucl Instrum Methods Phys Res Sect A. 2018;912:329–32.

111. Sharifi B, Saramad S. Investigation of a prototype double-stack MRPC detector with 20 gas gaps for Time-Of-Flight measurement in PET imaging systems. J Inst. 2020;15:P02015–P02015.

112. Gu Y, Levin CS. Study of electrode pattern design for a CZT-based PET detector. Phys Med Biol. 2014;59:2599–621.

113. Ariño-Estrada G, Mitchell GS, Kwon SI, Du J, Kim H, Cirignano LJ, et al. Towards time-of-flight PET with a semiconductor detector. Phys Med Biol. 2018;63:04LT01.

114. Ariño-Estrada G, Mitchell GS, Kim H, Du J, Kwon SI, Cirignano LJ, et al. First Cerenkov charge-induction (CCI) TlBr detector for TOF-PET and proton range verification. Phys Med Biol. 2019;64:175001.

115. Radogna R, Verwilligen P, Maggi M. Development of the FTM technology for TOF-PET. Nucl Instrum Methods Phys Res Sect A. 2019;936:449–50.

116. Pizzichemi M, Polesel A, Stringhini G, Gundacker S, Lecoq P, Tavernier S, et al. On light sharing TOF-PET modules with depth of interaction and 157 ps FWHM coincidence time resolution. Phys Med Biol. 2019;64:155008.

117. Gundacker S, Heering A. The silicon photomultiplier: fundamentals and applications of a modern solid-state photon detector. Phys Med Biol. 2020;65:17TR01.

118. Lv Y, Lv X, Liu W, Judenhofer MS, Zwingenberger A, Wisner E, et al. Mini EXPLORER II: a prototype high-sensitivity PET/CT scanner for companion animal whole body and human brain scanning. Phys Med Biol. 2019;64:075004.

119. Tai Y-C, Chatziioannou AF, Yang Y, Silverman RW, Meadors K, Siegel S, et al. MicroPET II: design, development and initial performance of an improved microPET scanner for small-animal imaging. Phys Med Biol. 2003;48:1519–37.

120. Melcher CL. Scintillation crystals for PET. J Nucl Med. 2000;41:1051–5.

121. Freedenberg MI, Badawi RD, Tarantal AF, Cherry SR. Performance and limitations of positron emission tomography (PET) scanners for imaging very low activity sources. Phys Med. 2014;30:104–10.

122. Bao Q, Chatziioannou AF. Estimation of the minimum detectable activity of preclinical PET imaging systems with an analytical method. Med Phys. 2010;37:6070–83.

123. van Eijk CWE. Inorganic scintillators in medical imaging. Phys Med Biol. 2002;47:R85-106.

124. Ren S, Yang Y, Cherry SR. Effects of reflector and crystal surface on the performance of a depth-encoding PET detector with dual-ended readout. Med Phys. 2014;41:072503.

125. Kang HG, Yamaya T, Han YB, Song SH, Ko GB, Lee JS, et al. Crystal surface and reflector optimization for the SiPM-based dual-ended readout TOF-DOI PET detector. Biomed Phys Eng Express. 2020;6:065028.

126. Stickel JR, Qi J, Cherry SR. Fabrication and characterization of a 0.5-mm lutetium oxyorthosilicate detector array for high-resolution PET applications. J Nucl Med. 2007;48:115–21.

127. Yoshida E, Hirano Y, Tashima H, Inadama N, Nishikido F, Moriya T, et al. The X'tal cube PET detector with a monolithic crystal processed by the 3D sub-surface laser engraving technique: performance comparison with glued crystal elements. Nucl Instrum Methods Phys Res Sect A. 2013;723:83–8.

128. Du J, Bai X, Cherry SR. Performance comparison of depth-encoding detectors based on dual-ended readout and different SiPMs for high-resolution PET applications. Phys Med Biol. 2019;64:15NT03.

129. Du J, Bai X, Cherry SR. A depth-encoding PET detector for high resolution PET using 1 mm SiPMs. Phys Med Biol. 2020;65:165011.

130. Yang Y, James SS, Wu Y, Du H, Qi J, Farrell R, et al. Tapered LSO arrays for small animal PET. Phys Med Biol. 2010;56:139–53.

131. Peng P, Liu C-C, Du J, Bai X, Cherry SR. Improving edge crystal identification in flood histograms using triangular shape crystals. Biomed Phys Eng Express. 2018;4:025031.

132. Joung J, Miyaoka RS, Lewellen TK. cMiCE: a high resolution animal PET using continuous LSO with a statistics based positioning scheme. Nucl Instrum Methods Phys Res Sect A. 2002;489:584–98.

133. Gonzalez-Montoro A, Gonzalez AJ, Pourashraf S, Miyaoka RS, Bruyndonckx P, Chinn G, et al. Evolution of PET detectors and event positioning algorithms using monolithic scintillation crystals. IEEE Trans Radiat Plasma Med Sci. 2021;5:1–1.

134. España S, Marcinkowski R, Keereman V, Vandenberghe S, Holen RV. DigiPET: sub-millimeter spatial resolution small-animal PET imaging using thin monolithic scintillators. Phys Med Biol. 2014;59:3405–20.

135. Zhang X, Wang X, Ren N, Hu B, Ding B, Kuang Z, et al. Performance of long rectangular semi-monolithic scintillator PET detectors. Med Phys. 2019;46:1608–19.

136. Yonggang W, Junwei D, Zhonghui Z, Yang Y, Lijun Z, Bruyndonckx P. FPGA based electronics for PET detector modules with neural network position estimators. IEEE Trans Nucl Sci. 2011;58:34–42.

137. Lecoq P, Gundacker S. SiPM applications in positron emission tomography: toward ultimate PET time-of-flight resolution. Eur Phys J Plus. 2021;136:292.

138. Gola A, Acerbi F, Capasso M, Marcante M, Mazzi A, Paternoster G, et al. NUV-sensitive silicon photomultiplier technologies developed at Fondazione Bruno Kessler. Sensors. 2019;19:308.

139. Yang Q, Wang X, Kuang Z, Zhang C, Yang Y, Du J. Evaluation of two SiPM arrays for depth-encoding PET detectors based on dual-ended readout. IEEE Trans Radiat Plasma Med Sci. 2020;5:1–1.

140. Schmall JP, Du J, Yang Y, Dokhale PA, McClish M, Christian J, et al. Comparison of large-area position-sensitive solid-state photomultipliers for small animal PET. Phys Med Biol. 2012;57:8119–34.

141. Peng Y, Lv W, Dai L, Zhao T, Liang K, Yang R, et al. A square-bordered position-sensitive silicon photomultiplier toward distortion-free performance with high spatial resolution. IEEE Electron Device Lett. 2020;41:1802–5.

142. Sacco I, Fischer P, Gola A, Piemonte C. A new position-sensitive silicon photomultiplier with submillimeter spatial resolution for photon-cluster identification. In: 2013 IEEE sensors; 2013. p. 1–4.

143. Du J, Schmall JP, Yang Y, Di K, Dokhale PA, Shah KS, et al. A simple capacitive charge-division readout for position-sensitive solid-state photomultiplier arrays. IEEE Trans Nucl Sci. 2013;60:3188–97.

144. Hatefi Hesari S, Haque MA, McFarlane N. A comprehensive survey of readout strategies for SiPMs used in nuclear imaging systems. Photonics. 2021;8:266.

145. Nadig V, Schug D, Weissler B, Schulz V. Evaluation of the PETsys TOFPET2 ASIC in multi-channel coincidence experiments. EJNMMI Phys. 2021;8:30.

146. Sánchez D, Gómez S, Mauricio J, Freixas L, Sanuy A, Guixé G, et al. HRFlexToT: a high dynamic range ASIC for time-of-flight positron emission tomography. IEEE Trans Radiat Plasma Med Sci. 2021;6:1–1.

147. Sacco I, Fischer P, Ritzert M. PETA4: a multi-channel TDC/ADC ASIC for SiPM readout. J Inst. 2013;8:C12013–C12013.

148. Schug D, Nadig V, Weissler B, Gebhardt P, Schulz V. Initial measurements with the PETsys TOFPET2 ASIC evaluation kit and a characterization of the ASIC TDC. IEEE Trans Radiat Plasma Med Sci. 2019;3:444–53.

149. Akamatsu G, Takyu S, Yoshida E, Iwao Y, Tashima H, Nishikido F, et al. Evaluation of a Hamamatsu TOF-PET detector module with 3.2 mm pitch LFS scintillators and a 256-channel SiPM array. IEEE Trans Radiat Plasma Med Sci. 2020;5:1–1.

150. Zhao Z, Huang Q, Gong Z, Su Z, Moses WW, Xu J, et al. A novel read-out electronics design based on 1-bit sigma-delta modulation. IEEE Trans Nucl Sci. 2017;64:820–8.

151. Cheng X, Hu K, Shao Y. Dual-polarity SiPM readout electronics based on 1-bit sigma-delta modulation circuit for PET detector applications. IEEE Trans Nucl Sci. 2019;66:2107–13.

152. Won JY, Ko GB, Kim KY, Park H, Lee S, Son J-W, et al. Comparator-less PET data acquisition system using single-ended memory interface input receivers of FPGA. Phys Med Biol. 2020;65:155007.

153. Average human height by country. Wikipedia; 2021. https://en.wikipedia.org/w/index.php?title=Average_human_height_by_country&oldid=1032217037. Cited 24 Jul 2021.

154. Moses WW. Fundamental limits of spatial resolution in PET. Nucl Instrum Methods Phys Res Sect A. 2011;648:S236–40.

155. Levin CS, Hoffman EJ. Calculation of positron range and its effect on the fundamental limit of positron emission tomography system spatial resolution. Phys Med Biol. 1999;44:781–99.

156. Yamamoto S, Yeom JY, Kamada K, Endo T, Levin CS. Development of an ultrahigh resolution block detector based on 0.4 mm pixel Ce:GAGG scintillators and a silicon photomultiplier array. IEEE Trans Nucl Sci. 2013;60:4582–7.

157. Mohammadi I, Castro IFC, Correia PMM, Silva ALM, Veloso JFCA. Minimization of parallax error in positron emission tomography using depth of interaction capable detectors: methods and apparatus. Biomed Phys Eng Express. 2019;5:062001.

158. Stockhoff M, Decuyper M, Van Holen R, Vandenberghe S. High resolution monolithic LYSO detector with 6-layer depth-of-interaction for clinical PET. Phys Med Biol. 2021;66:155014.

159. Bläckberg L, Sajedi S, Fakhri GE, Sabet H. A layered single-side readout depth of interaction time-of-flight-PET detector. Phys Med Biol. 2021;66:045025.

160. Peng P, Zhang M, Zeraatkar N, Qi J, Cherry SR. Tomographic imaging with Compton PET modules: ideal case and first implementation. J Inst. 2021;16:T04007.

161. Ito M, Hong SJ, Lee JS. Positron emission tomography (PET) detectors with depth-of- interaction (DOI) capability. Biomed Eng Lett. 2011;1:70.

162. Akamatsu G, Tashima H, Iwao Y, Wakizaka H, Maeda T, Mohammadi A, et al. Performance evaluation of a whole-body prototype PET scanner with four-layer DOI detectors. Phys Med Biol. 2019;64:095014.

163. Nitta M, Inadama N, Nishikido F, Yoshida E, Tashima H, Kawai H, et al. Development of the X'tal cube PET detector with segments of (0.77 mm)3. IEEE Trans Radiat Plasma Med Sci. 2018;2:564–73.

164. Zhang Y, Yan H, Baghaei H, Wong W-H. A novel depth-of-interaction block detector for positron emission tomography using a dichotomous orthogonal symmetry decoding concept. Phys Med Biol. 2016;61:1608–33.

165. Son J-W, Lee MS, Lee JS. A depth-of-interaction PET detector using a stair-shaped reflector arrangement and a single-ended scintillation light readout. Phys Med Biol. 2016;62:465–83.

166. Moses WW, Derenzo SE. Design studies for a PET detector module using a PIN photodiode to measure depth of interaction. IEEE Trans Nucl Sci. 1994;41:1441–5.

167. Choghadi MA, Huang SC, Shimazoe K, Takahashi H. Evaluation of dual-ended readout GAGG-based DOI-PET detectors with different surface treatments. Med Phys. 2021;48:3470–8.

168. Snyder DL, Thomas LJ, Ter-Pogossian MM. A mathematical model for positron-emission tomography systems having time-of-flight measurements. IEEE Trans Nucl Sci. 1981;28:3575–83.

169. Budinger TF. Time-of-flight positron emission tomography: status relative to conventional PET. J Nucl Med. 1983;24:73–8.

170. Tomitani T. Image reconstruction and noise evaluation in photon time-of-flight assisted positron emission tomography. IEEE Trans Nucl Sci. 1981;28:4581–9.

171. Schaart DR, Schramm G, Nuyts J, Surti S. Time of flight in perspective: instrumental and computational aspects of time resolution in positron emission tomography. IEEE Trans Radiat Plasma Med Sci. 2021;5:1–1.

172. Kwon SI, Ota R, Berg E, Hashimoto F, Nakajima K, Ogawa I, et al. Ultrafast timing enables reconstruction-free positron emission imaging. Nat Photonics. 2021;15:914–8.

173. Gundacker S, Turtos RM, Kratochwil N, Pots RH, Paganoni M, Lecoq P, et al. Experimental time resolution limits of modern SiPMs and TOF-PET detectors exploring different scintillators and Cherenkov emission. Phys Med Biol. 2020;65:025001.

174. Wagadarikar AA, Ivan A, Dolinsky S, McDaniel DL. Sensitivity improvement of time-of-flight (ToF) PET detector through recovery of Compton scattered annihilation photons. IEEE Trans Nucl Sci. 2014;61:121–5.

175. Yoshida E, Tashima H, Yamaya T. Sensitivity booster for DOI-PET scanner by utilizing Compton scattering events between detector blocks. Nucl Instrum Methods Phys Res Sect A. 2014;763:502–9.

176. Lee S, Kim KY, Lee MS, Lee JS. Recovery of inter-detector and inter-crystal scattering in brain PET based on LSO and GAGG crystals. Phys Med Biol. 2020;65:195005.

177. Hsu DFC, Freese DL, Innes DR, Levin CS. Intercrystal scatter studies for a 1 mm3 resolution clinical PET system prototype. Phys Med Biol. 2019;64:095024.

178. Surti S, Karp JS. Impact of event positioning algorithm on performance of a whole-body PET scanner using one-to-one coupled detectors. Phys Med Biol. 2018;63:055008.

179. Gillam JE, Solevi P, Oliver JF, Casella C, Heller M, Joram C, et al. Sensitivity recovery for the AX-PET prototype using inter-crystal scattering events. Phys Med Biol. 2014;59:4065–83.

180. Michaud J-B, Tétrault M-A, Beaudoin J-F, Cadorette J, Leroux J-D, Brunet C-A, et al. Sensitivity increase through a neural network method for LOR recovery of ICS triple coincidences in high-resolution pixelated-detectors PET scanners. IEEE Trans Nucl Sci. 2015;62:82–94.

181. Pratx G, Levin CS. Bayesian reconstruction of photon interaction sequences for high-resolution PET detectors. Phys Med Biol. 2009;54:5073–94.

182. Spencer BA, Berg E, Schmall JP, Omidvari N, Leung EK, Abdelhafez YG, et al. Performance evaluation of the uEX-PLORER total-body PET/CT scanner based on NEMA NU 2-2018 with additional tests to characterize PET scanners with a long axial field of view. J Nucl Med. 2021;62:861–70.

183. Carter LM, Kesner AL, Pratt EC, Sanders VA, Massicano AVF, Cutler CS, et al. The impact of positron range on PET resolution, evaluated with phantoms and PHITS Monte Carlo simulations for conventional and non-conventional radionuclides. Mol Imaging Biol. 2020;22:73–84.

184. Herraiz JL, Bembibre A, López-Montes A. Deep-learning based positron range correction of PET images. Appl Sci. 2021;11:266.

185. Conti M, Eriksson L, Rothfuss H, Sjoeholm T, Townsend D, Rosenqvist G, et al. Characterization of176Lu background in LSO-based PET scanners. Phys Med Biol. 2017;62:3700–11.

186. Huesman RH, Klein GJ, Moses WW, Qi J, Reutter BW, Virador PRG. List-mode maximum-likelihood reconstruction applied to positron emission mammography (PEM) with irregular sampling. IEEE Trans Med Imaging. 2000;19:532–7.

187. Bloomfield PM, Rajeswaran S, Spinks TJ, Hume SP, Myers R, Ashworth S, et al. The design and physical characteristics of a small animal positron emission tomograph. Phys Med Biol. 1995;40:1105–26.

Publisher's Note

Springer Nature remains neutral with regard to jurisdictional claims in published maps and institutional affiliations.